fire_cci

D3.6.2 - Algorithm Theoretical Basis Document – Volume II – BA Algorithm Development

ATBD II, BA Algorithm Development, version 2

Project Name	ESA CCI ECV Fire Disturbance (fire_cci)
Contract N°	4000101779/10/I-NB
Project Manager	Arnd Berns-Silva
Last Change Date	09/09/2014
Version	2.2
State	Final
Author	José Miguel Cardoso Pereira, Bernardo Mota, Teresa Calado, Itziar Alonso, Patricia Oliva, Federico González-Alonso
Document Ref:	Fire_cci_Ph3_ISA_D3_6_2_ATBD_II_v2_2
Document Type:	Public

Project Partners

Prime Contractor/ **Scientific Lead**	-	UAH - University of Alcalá de Henares (Spain)
Project Management	-	GAF AG, (Germany)
System Engineering Partners	- -	GMV - Aerospace & Defence (Spain) DLR - German Aerospace Centre (Germany)
Earth Observation Partners	- - - -	INIA-CIFOR (Spain) ISA - Instituto Superior de Agronomia (Portugal) UL - University of Leicester (United Kingdom) DLR – German Aerospace Centre (Germany)
Climate Modelling Partners	- - -	IRD-CNRS - L'Institut de Recherche pour le Développement - Centre National de la Recherche Scientifique (France) JÜLICH - Forschungszentrum Jülich GmbH (Germany) LSCE - Laboratoire des Sciences du Climat et l'Environnement (France)

Distribution

Affiliation	Name	Address	Copies
ESA - ECSAT	Stephen Plummer (ESA – ECSAT)	Stephen.Plummer@esa.int	electronic copy
Project Team	Emilio Chuvieco, (UAH) Itziar Alonso (UAH) Stijn Hantson (UAH) Marc Padilla Parellada (UAH) Dante Corti (UAH) Arnd Berns-Silva(GAF) Christopher Sandow (GAF) Stefan Saradeth (GAF) Jose Miguel Pereira (ISA) Bernardo Mota (ISA) Gerardo López Saldaña (ISA) Kevin Tansey (UL) Oscar Pérez (GMV) Luis Gutiérrez (GMV) Ignacio García Gil (GMV) Andreas Müller (DLR) Martin Bachmann (DLR) Kurt Guenther (DLR) Veronika Gstaiger (DLR) Eric Borg (DLR) Martin Schultz (JÜLICH) Angelika Heil (JÜLICH) Florent Mouillot (IRD) Philippe Ciais (LSCE) Patricia Cadule (LSCE) Chao Yue (LSCE)	Emilio.chuvieco@uah.es itziar.alonsoc@uah.es Hantson.stijn@gmail.com padilla.marc@gmail.com dante.corti@uah.es arnd.berns-silva@gaf.de christopher.sandow@gaf.de stefan.saradeth@gaf.de jmocpereira@gmail.com bmota@isa.utl.pt gerardoLopez@isa.utl.pt kjt7@le.ac.uk operez@gmv.com lgutierrez@gmv.com igarcia@gmv.com andreas.mueller@dlr.de martin.bachmann@dlr.de kurt.guenther@dlr.de Veronika.Gstaiger@dlr.de eric.borg@dlr.de m.schultz@fz-juelich.de a.heil@fz-juelich.de florent.mouillot@ird.fr philippe.ciais@cea.fr patricia.cadule@lsce.ipsl.fr chaoyuejoy@yahoo.com.cn	electronic copy

Summary

This document is the Algorithm Theoretical Basis Document Volume II version 2 for the fire_cci project holding a final detailed description of the algorithms developed and implemented into the fire_cci prototype processing chain.

	Affiliation/Function	Name	Date
Prepared	ISA, UAH, INIA	José Miguel Cardoso Pereira, Bernardo Mota, Itziar Alonso Federico González-Alonso	11/08/2013 02/12/2013 05/09/2014
Reviewed	UAH, GAF	Emilio Chuvieco, Arnd Berns-Silva	09/09/2014
Authorized	UAH/ Prime Contractor	Emilio Chuvieco	
Accepted	ESA/ Project Manager	Stephen Plummer	

Signatures

	Name	Date	Signature
Signature of authorisation and overall approval	Emilio Chuvieco		
Signature of acceptance by ESA			

Document Status Sheet

Issue	Date	Details
1.0	12/06/2012	First Document Issue
1.1	11/01/2013	Addressing ESA comments according to CCI-FIRE-EOPS-MM-12-0046.pdf
2.0	16/08/2013	Holding updated and final algorithm developments
2.1	10/12/2013	Addressing ESA comments according CCI-FIRE-EOPS-MM-13-0037.pdf

Document Change Record

#	Date	Request	Location	Details
1.1	11/01/2013	ISA	Section 2	Changing sub-sections index for "Heat" and "Smoke"; Renaming sub-section "Burned Area" into "Scar"
			Section 3.3.2	Paragraph shortened
			Section 3.6	Introducing chapter "Conclusions"
			Section 4.1	Introducing general statement
			Section 4.1.1.3	Introducing paragraph referring to scientific papers on MRF
			Section 4.3.3	Restructuring of sub-sections Elaborating on post-fire composites and annual trends
			Section 4.3.3.1	Restructuring and elaborating annual reference trends
2.0	12/08/2013	ISA	Section 4.2, Figure 3	Updating BA classification and mapping algorithm
			Section 4.2.1.3.1	Introducing sub-section "Compromise programming"
			Section 4.2.1.3.2, page 23	Introducing sub-section "Selection of changepoints in single-pixel time series" Introducing Figure 12
			Section 4.2.1.3.3	Introducing sub-section "Fire seasonality score"
			Section 4.2.1.3.4	Introducing sub-section "Scoring annual changepoint maps"
			Page 24 – 25	Introducing Figures 13, 14, 15, 16
			Section 4.2.1.4.3	Introducing Figure 18
			Section 4.3	Updating and further remarks
			Section 4.3.1	Updating and further remarks
			Page 29	Updating Figure 19
			Page 32	Introducing Figure 23
			Page 33	Introducing description to Table 2,3 and 4
			Section 4.3.3.1	Introducing chapter "Compositing length"
			Section 4.3.3.2	Introducing chapter "Post-fire composites"
			Section 4.3.3.3	Introducing chapter "Closest day to the HS"
			Page 36	Introducing Figure 26, 27, 28
			Section 4.3.3.4	Introducing chapter "2nd NIR minima"
			Page 37	Introducing Figure 29, 30
			Section 4.3.3.5	Introducing chapter "Final compositing criterion"
			Page 38	Introducing Figure 31, 32
			Section 4.3.4	Introducing Figure 33
			Section 4.3.5.1	Introducing chapter "Criteria for selecting seed pixels"
			Page 39	Introducing Figure 34
			Section 4.3.5.2	Introducing chapter "Identification of burned statistics
			Page 40	Introducing Figure 35
			Page 41	Introducing Figure 36
			Section 4.3.5.3	Introducing chapter "Final seed selection"
			Page 41	Updating Figure 37
			Section 4.3.6	Updating and further remarks
			Page 42	Updating Figure 38

#	Date	Request	Location	Details
			Section 4.4	Updating and further remarks
			Page 43	Updating Figure 39, Introducing Figure 40
			Page 44	Introducing Figure 41, 42
			Page 45	Introducing Table 5
2.1	10/12/2013	ISA,UAH	Section 1.1	Rephrasing text;
			Section 2.1.3	Rephrasing text;
			Section 3.5, 2nd paragraph	Rephrasing text;
			Section 4.1, 4.2	Rephrasing text; Updating bibliography
			Section 4.2.1.3.4	Updating annotation of Figure 13 and 14
			Section 4.3	Rephrasing and updating text;
			Section 4.3.1	Updating Figure 20
			Section 4.3.2	Updating Figure 22; Updating annotation of Figure 23
			Section 4.3.3.5	Updating Figure 30
			Section 4.3.5.2	Updating annotation Figure 33
2.2	06/09/2014	ISA,UAH	Section 4.2.1.2	Updated references; Adoption of Changepoint detection
			Section 4.2.1.3	Updating changepoint selection and scoring
			Section 4.2.1.4	Rephrasing
			Section 4.3.2	Introducing chapter "Generation of spectral indices" separately
			Section 4.3.3	Indicating HS value extraction from Thiessen matrix
			Section 4.3.4.5	Updating composition criterion
			Section 4.3.5	Updated description of GEMI
			Section 4.3.6.1	Introducing additional temporal change constraint
			Section 4.3.6.2	Upgrading Identification of burned statistics; Updating Figure 33
			Section 4.3.6.3	Updating Final seed selection
			Section 4.3.7	Upgrading Region growing
			Whole document	Typo/grammar corrections and rephrasing; Tables renumbered; Updating references

Table of Contents

List of Tables

List of Figures

List of Abbreviations

AATSR	Advanced Along-Track Scanning Radiometer
AD	Applicable Document
ASAR	Advanced Synthetic Aperture Radar
ATBD	Algorithm Theoretical Basis Document
ATSR-2	Along-Track Scanning Radiometer
AVHRR	Advanced Very High Resolution Radiometer
AWiFS	Advanced Wild Field Sensor
BA	Burned Area
BAI	Burned Area Index
BASA	Burned Area Synergic Algorithm
BRDF	Bidirectional Reflectance Distribution Function
CART	Classification And Regression Trees
CCI	Climate Change Initiative
CP	Compromise Programming
CPD	Change Point Detection
DARD	Data Access Requirements Document
ENVISAT	ENVIronmental SATellite
ESA	European Space Agency
ECV	Essential Climate Variables
FAO	Food and Agriculture Organization
FR	Full Resolution
GBA	Global burned Area
GCOS	Global Climate Observing System
GEMI	Global Environmental Monitoring Index
HS	HotSpot
IPCC	Intergovernmental Panel on Climate Change
JRC	Joint Research Centre
MCDA	Multi-Criteria Decision Analysis
MEF	Model Efficiency Index
MERIS	MEDium Resolution Imaging Spectrometer
MLP	Multi-Layer Perceptron
MODIS	Moderate Resolution Imaging Spectroradiometer
MIR	Mid-InfraRed
MRF	Markov Random Field
NASA	National Aeronautics and Space Administration
NDVI	Normalized Difference Vegetation Index
NIR	Near-InfraRed
NOAA	National Oceanic and Atmospheric Administration
PELT	Pruned Exact Linear Time
QUEST	Quick, Unbiased, Efficient Statistical Trees
R	Red
"R"	R software environment for statistical computing
RR	Reduced Resolution
SAI	Spectral Angle Images
SPOT	Satellite Pour l'Observation de la Terre
SVM	Support Vector Machine
SWIR	Short-Wave InfraRed
TIR	Thermal InfraRed
UTL	Technical University of Lisbon
VEGETATION	CNES Earth's observation sensor onboard SPOT-4/SPOT-5
VIS	VISible

1 Executive Summary

1.1 Purpose of the document

The importance of fire in e.g. the emissions of greenhouse gases and aerosols, the carbon cycle and land cover changes, led to the need of high quality, long-term burned area estimates. On the other hand, the global warming as a result of increases of radiative gases (e.g. CO_2, CH_4) in the atmosphere caused by human activities (IPCC 2007) may have a profound impact on fire activity. In fact, the apparent global increase in the incidence, extent and severity of uncontrolled burning led to calls for international environmental policies concerning fire (FAO 2007).

The use of remote sensing allowed a remarkable development of burned area mapping on regional and global scales, since instruments on-board satellites are currently the only available operational systems capable to collect cost-effective burned area information at adequate spatial and temporal resolutions (Chuvieco, 2008).

The importance of fire on environmental studies and Earth resources management activities together with the availability of remote sensing data led to the growing number of multi-year, global burned area products, such as Global Burned Area (GBA) 2000 (Tansey et al. 2004), L3JRC (Tansey et al. 2008), GLOBSCAR (Simon 2004), the 1-km GLOBCARBON burned area product (Plummer et al. 2006), the AQL2004 project developed by RedLaTIF (Chuvieco et al. 2008a) and MCD45A1 product (Roy et al. 2008).

The Algorithm Theoretical Basis Document (ATBD), vol. II, describes in detail the burned area algorithms developed using the multi-sensor data archives from AATSR, VGT and MERIS FRS. These algorithms currently are adapted to the specifications of European sensors (A)ATSR, VEGETATION and MERIS, which are the core of fire_cci. In this first project phase data are analysed for the periods 1995-2009 time series for specific test sites (see Calado et al. 2011), along with global mosaics for specific years.

This version of the document presents the final algorithms developed by the (A)ATSR / VGT and MERIS teams. Following the CCI Statement of Work [AD-1], this document evolved during the progress of the project.

1.2 Applicable Documents

[AD-1]	ESA Climate Change Initiative (CCI) Phase 1, Scientific User Consultation and Detailed Specification, Statement of Work, EOP-SEP/SOW/0031-09/SP, v1.4, 2009, https://www.esa-fire-cci.org/webfm_send/110

1.3 Document Structure

The fire_cci ATBD is structured as follows:

Section 1 is the Executive Summary.

Section 2 is the state of the art and focus on several aspects related to fires.

Section 3 gives an overview of the existing global burned area products, including product comparison.

Section 4 describes the (A)ATSR, VGT and MERIS algorithms for burned area detection.

Section 5 contains the references.

2 Introduction

2.1 State of the Art

Burned Area (BA) is the primary variable of the fire disturbance ECV and is part of the ESA Climate Change Initiative (CCI) programme. The programme aims at taking full advantage of the long-term global Earth Observation archives that ESA and its Member states have established over the last years, in the generation of ECV databases as stated by the Global Climate Observing System (GCOS, 2009). Accordingly, the fire_cci project shall focus on the generation of burned area (BA) products, that will be adapted to the climate modelling community, using (A)ATSR, VEGETATION and MERIS data.

2.1.1 Remote sensing of fire signals

Wildfire generates various types of remotely sensed signal as a result of the biomass combustion process. Some fire effects, such as heat and smoke last for relatively short periods of time. Others, like the char residue left on the surface, and especially the altered vegetation structure are more persistent (Robinson 1991; Pereira et al., 1999b). Surface charring is a quite unique consequence of vegetation combustion, but has relatively short duration and tends to be strongly attenuated by wind and rainfall in a few weeks or months after the fire. Burned patches and vegetation removal by fire are more stable (although its persistence may vary from a few weeks in tropical grasslands, to decades in boreal forest ecosystems), but less significant to discriminate fire effects, since partial or complete removal of plant canopies also may be due to other factors such as harvesting, grazing, wind throw, water stress, or the action of insects and pathogens.

2.1.2 Char

The consumption of plant biomass by fire leaves charcoal on the ground is one of its most abundant residues. The magnitude and direction of spectral changes caused by the surface charring depends on the condition of the vegetation prior to burning. In ecosystems dominated by herbaceous vegetation (e.g. savannas, steppe, grasslands), there is a marked annual phenological cycle, and the aboveground plant parts typically are dead and dry at the time fires occur. The major spectral change is a sharp decrease in surface reflectance over the entire 0.4 - 3μm region, i.e., from bright dry grass to charred soil surface. By contrast, in most forests and shrub lands, the aboveground vegetation is live and green during the fire season. In this case, the drop in NIR reflectance tends to be smaller than in savannas, steppes and grasslands. Spectral reflectance changes in the SWIR are more complex, because tall, dense vegetation is dark and replacing this kind of land cover by a charcoal layer may not darken the surface much further. When a bright soil background is exposed as a result of the fire-induced erosion, SWIR surface reflectance may display a small increase. Spectral signatures of charcoal, green vegetation and dry vegetation are shown in Figure 1.

Pereira et al. (1999b) provided an overview of the spectral properties of burned areas in the spectral range from visible to microwave, and covering various biomes. They indicate that the visible spectral range is not very effective for discriminating burns and suggest various reasons: 1) Like recent burns, several common land cover types, namely water bodies, wetlands, dense conifer forests, and many soil types are quite dark in the visible. These similarities reduce the possibility of using the visible range to discriminate burns; 2) The dynamic range available with Earth observation satellites for discriminating between these different types of surfaces, all of which are dark in the visible, is narrow; 3) path radiance, an important component of the atmospheric effect, predominates in the visible range especially over dark surfaces, and causes a loss of contrast between different land cover types.
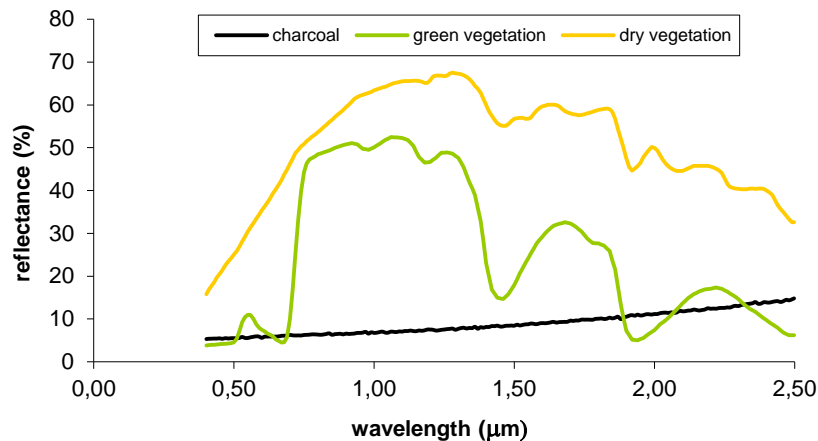
Figure 1: Typical spectral reflectance signatures of pure charcoal, green vegetation and dry vegetation

The NIR is the spectral region where the signal of recent burned area (BA) is strongest and, therefore NIR is considered as the best spectral region for BA detection and mapping, especially when pre-fire fuel loadings are high and combustion produces large amounts of charcoal that are deposited on the ground. Since green vegetation is very reflective in the NIR, burning typically causes significant decreases in reflectance. The phenological status of the vegetation (i.e. green *versus* dry) prior to the fire appears to be of little relevance in the NIR, and therefore does not introduce a distinction between the burning of dry savannas on one side, and the burning of green forests and shrub lands, on the other side. Both green and dry vegetation have substantially higher reflectance than recent burns, and therefore darkening of the burned surfaces in the NIR is quite systematic.

SWIR spectral changes induced by fire are similar to those in the visible range, since burned areas are typically more reflective than green vegetation, but darker than the predominantly senesced vegetation of tropical savannas during the dry season. Pereira (1999) found that the change in reflectance over burned surfaces is higher in the SWIR than in the visible, and thus considered the NIR - SWIR bispectral space more appropriate for burned area discrimination and mapping than the classical visible (VIS) - NIR space used in remote sensing of vegetation. The already mentioned higher smoke aerosol transmittance in the SWIR is an additional advantage of the NIR – SWIR bi-spectral space.

Trigg and Flasse (2000) reached similar conclusions in a field spectroradiometry study of burns in southern African grassland. In particular, they found that 0.86µm and 1.24µm reflectance displays substantial reflectance decrease for at least 13 days after the burn; red, green and SWIR (1.65 µm) are mostly sensitive immediately after the burn; SWIR (2.1µm) becomes sensitive from one day after the burn; blue is insensitive to burning. Spectral differences between pre- and post-fire (signal) become statistically insignificant in the green, SWIR (1.6 µm) and red bands, respectively at seven, seven and eleven days after the fire. Fuel loading of the study area was very low (0.35 t.ha^{-1}) and areas with higher fuel loadings are expected to produce more abundant combustion products and a more persistent burn signal. Trigg and Flasse (2001) compared various bi-spectral spaces defined with MODIS channels for the discrimination of burned areas from a range of land cover types in southern African savannas. They found that the best bi-spectral space was defined by the 1.65 µm and 2.1 µm channels. Bi-spectral spaces involving the visible range perform worse than those defined in the NIR-SWIR or SWIR-SWIR spaces. The AATSR and SPOT-VGT afford a limited choice of bi-spectral spaces, the best performing of which, according to this analysis ought to be that defined in the NIR-SWIR (e.g. 0.86 µm – 1.65 µm). However, Trigg and Flasse (2001) comment that it performs better for the discrimination of burns in green vegetation than in senescent vegetation. However, field spectroradiometric data from southern African grassland and woodland ecosystems reported by Pereira (2003) show a substantially larger fire-induced spectral change in the (senescent) grassland than in the woodland. SWIR behaviour illustrates previous statements of low sensitivity to burning in green vegetation.

Silva et al. (2004) specifically addressed the issue of fire-induced spectral reflectance changes as a function of pre-fire vegetation phenology (quantified with the NDVI), using SPOT-VGT data from study areas in boreal forests, tropical savannas, and temperate forests and shrub lands. NIR reflectance was found to decrease markedly after burning in all land cover types considered in the three different study areas. All burned areas in the grasslands and croplands showed NIR and SWIR reflectance decrease. In evergreen needle leaf forest, mixed forest, woodland and wooded grassland, spectral changes induced by fire displayed two distinct responses: a simultaneous decrease of SWIR and NIR reflectance; or a small increase in SWIR reflectance and a decrease in NIR reflectance. The expected post-fire decrease in SWIR reflectance, owing to strong absorption by charcoal (Pereira et al. 1999a, Fraser et al. 2000), occurs mostly in dry vegetation, such as grassland, which has high pre-fire SWIR reflectance. In contrast, green vegetation, which has low pre-fire SWIR reflectance due to high moisture content, displays smaller reflectance changes due to burning (Figure 2). In very green vegetation, burning may even cause a small increase in SWIR reflectance (Silva et al. 2004).
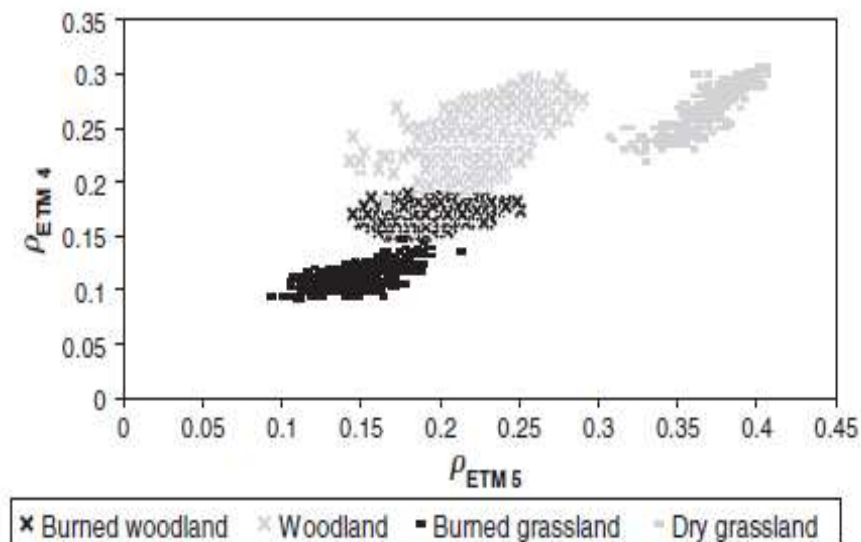
Figure 2: Fire-induced spectral reflectance changes in a mid-infrared (ρETM5, 1.65µm) *versus* near-infrared (ρETM4, 0.86µm) bi-spectral space. Data from a Landsat 7 Enhanced Thematic Mapper scene from the Western Province, Zambia, dated September 2000 (Pereira 2003).

2.1.3 Scar

Fire alters the vegetation structure by consuming leaves, twigs and fine branches. The resulting spectral changes last longer than those caused by the deposition of ash and charcoal. Persistence of the fire scar signal is a function of vegetation type, net primary productivity and plant succession dynamics, and may range from a few weeks in tropical grasslands to decades in boreal forests. Modifications of the three dimensional structure of vegetation affect its shading pattern, while consumption of photosynthetically active plant parts eliminates the greenness signal. The soil background exposed by vegetation removal will also contribute to the overall spectral signal of the fire-affected area. This is, however, dependent on severity. If a stand replacing fire occurs, then shadowing can be neglected. In a ground fire, only the surface vegetation layer at the bottom is affected, and thus the signal is weak and of ephemeral.Considering the specifications of the present project, which relies on daily, or near-daily data for the detection of burned areas, the post-fire signal is expected to be strongly dominated by the char signal.

2.1.4 Heat

Both the (A)ATSR / VGT and the MERIS algorithm incorporate active fire data, based on sensing the heat from vegetation burning, hence this brief overview of the thermal signal. Temperatures of 1000°K and 600°K can be assumed as representative of typical flaming and smouldering combustion phases of vegetation fires, respectively (Lobert and Warnatz 1993). According to Wien's Displacement Law, the

peak emission of radiance for flames and smouldering surfaces would be located in the middle infrared (MIR), between 3μm and 5μm. For an ambient temperature of 290°K (17°C), the peak of radiance emission is located at approximately 10μm. Active fire detection from remote sensing exploits this behaviour, and typically relies on some combination of brightness temperature measured in the 3μm - 5μm and 10μm - 12μm regions. The key "active fire signal" is, therefore, an increase of the observed radiance in the 3μm - 5μm region, relatively to surrounding areas. For increasingly smaller and/or cooler fires, this contrast is progressively attenuated and becomes difficult to discriminate from natural spatial variability of the land surface temperature field. Additional perturbation sources for active fire detection may be the presence of atmospheric water vapour, a strong reflection of solar radiation in the 3μm - 5μm region, or the presence of sub-pixel clouds (Kaufman and Justice 1998).

2.1.5 Smoke

Smoke from vegetation burning often interferes with observation of the land surface, influencing the choice of the spectral domains of observation, and affecting burned area mapping timeliness and accuracy. Data pre-processing for this project incorporated screening of smoke-contaminated imagery, but residual contamination may be present in the data used by the BA classification algorithms, which is why the smoke signal is addressed here. Biomass burning in wildfires is not fully efficient, due to high fuel moisture, insufficient oxygenation of the reaction zone, inefficient heat transfer, etc. The more efficient phase of flaming combustion yields products such as char (partially oxidised wood) coexists with less efficient smouldering combustion, the phase that takes place behind the active flame front and yields substantial amounts of smoke. Since the objective is to detect and map fire effects at the land surface, smoke is seen as an atmospheric disturbance that interferes with this objective. Mie scattering is strongest when particle radius corresponds to the wavelength of radiation. Smoke aerosol particles range in size from 0.01 to 1.0μm, which makes them efficient scatterers of solar radiation (Jacob 1999). Biomass burning smoke is also an absorbing aerosol, because it contains high concentrations of black carbon (Dubovik et al. 2002; Kaufman et al. 2002). The perturbation caused by smoke aerosol to observation of the land surface from satellite can be quantified calculating the aerosol transmittance, $\tau_{a\lambda}$ (Iqbal 1983), which increases strongly with wavelength. Smoke aerosol transmittance is very low in the visible spectral domain, which becomes inadequate to monitor the land surface when biomass burning emissions are present in the atmosphere in significant amounts. Under such circumstances burned area mapping is better accomplished using near-infrared (NIR: 0.7-1.2 μm) and shortwave-infrared (SWIR, 1.4-2.5 μm) spectral data (Kaufman et al. 1997; Pereira 1999, 2003).

3 Overview of pre-existing global burned area products

Several methods based on remote sensing imagery for continental and global burned area mapping have been developed in the past few years (Barbosa et al. 1999, Roy et al. 2002, Govaerts et al. 2002, Tansey et al. 2004, Giglio et al. 2009), using a variety of change detection techniques. This is a complex problem, for a number of reasons, such as the dependence of the burned area spectral signature on the type and quantity of vegetation burned, variable burn severity and combustion completeness, the post fire rates of combustion product (charcoal and ash) scatter and vegetation recovery rate. First a brief overview of global burned area products based on the AVHRR and MODIS sensors is given, followed by a more detailed analysis of products derived from (A)ATSR and SPOT-VGT imagery (*see* sections 3.3 and 3.4, respectively). Also studies to assess the capability of MERIS for BA detection are addressed (*see* section 3.5).

3.1 AVHRR-based global burned area products

Carmona-Moreno et al. (2005) used daily global observations from the NOAA/AVHRR between 1982 and 1999 to create a weekly global burned area product at 8km spatial resolution. The algorithm for identifying burned surfaces uses data from AVHRR channels 1–3, extending the approach of Barbosa et al. (1999a, b). Comparison with independently available fire data indicate that the time-series is inadequate to make quantitative and accurate estimates of global burned area, it is suitable to assess changes in location and season of burning at the global scale. Fire seasonality and fire distribution data sets were integrated as 0.5º fire probability grid maps.

Riaño et al. (2007) analysed spatial and temporal patterns of global burned area with the Daily Tile US NOAA/AVHRR Pathfinder 8 km Land dataset between 1981 and 2000. Burned area mapping relied on algorithms previously developed for Africa by Barbosa et al. (1999b) and Moreno-Ruiz et al. (1999), but using imagery which addressed the solar zenith angle errors affecting previous datasets. The studied focused on the identification of large scale fire seasonality patterns in the northern and southern hemispheres, and on the detection of regional trends in burned area extent.

Even with the solar zenith angle correction, the Pathfinder 8km dataset still is affected by spurious temporal trends, which limit the temporal consistency of burned area products. Its low spatial resolution very likely leads to substantial underestimation of area burned in extensive areas of the planet. The global burned area products of Carmona-Moreno et al. (2005) and Riaño et al. (2007) both apply, at the global scale, an algorithm originally developed to map burns over Africa, which may also lead to higher inaccuracies over temperate and boreal regions.

3.2 MODIS-based global burned area products

Roy et al. (2002) inverted a bi-directional reflectance model against multi-temporal land surface reflectance data, obtaining expectation and uncertainty estimates of subsequent observations through time. Their algorithm deals with angular variations in multi-temporal data and use a statistical measure to detect change from a previously state. Large discrepancies between predicted and observed values are attributed to change. A temporal consistency threshold is used to differentiate between sporadic changes, considered as noise, and persistent changes interpreted as burns. The algorithm is adaptive to the number, viewing and illumination geometry of the observations, and to the level of data noise. Roy et al. (2008) presented first results of this algorithm for 12 consecutive months of the NASA Moderate Resolution Imaging Spectroradiometer (MODIS) global burned area product. Globally the total area burned detected by the MODIS product was 3.66×10^6 km^2 for July 2001 to June 2002. Comparison with the MODIS global active fire product showed that the MODIS burned area product labels a greater proportion of the landscape as burned Globally, the burned area product reports a smaller amount of area burned than the active fire product in croplands and evergreen forest and deciduous needle leaf forest classes, comparable areas for mixed and deciduous broadleaf forest classes, and a greater amount of area burned for the non-forest classes.

Giglio et al. (2006) proposed a method for estimating monthly burned area globally at 1° spatial resolution, with MODIS Terra imagery and ancillary vegetation cover information. They constructed regression trees for 14 different global regions, calibrating MODIS active fire observations to burned area estimates from MODIS 500-m imagery, assuming proportionality between burned area and active fire counts. Regional regression trees were applied to the full archive of MODIS Terra fire data, yielding a monthly global burned area product ranging from late 2000 through mid-2005. Annual burned area estimates thus derived compare well with independent annual estimates for Canada, the United States, and Russia. Global annual burned area estimates for the years 2001–2004 varied between 2.97 million and 3.74 million km^2, with the maximum in 2001.

3.3 (A)ATSR-based global burned area products

There is significant previous experience with the use of (A)ATSR data for burned area mapping at the global scale. A brief overview of methods, results and assessment of the two available global burned area products developed from these sensors is provided below.

3.3.1 GlobScar

The European Space Agency GlobScar Project produced global monthly burned area maps at 1km spatial resolution using day-time data of the Along Track Scanning Radiometer (ATSR-2) instrument onboard the ESA ERS-2 satellite from the year 2000. The image classification procedure combines two distinct algorithms: K1 is a contextual algorithm based on the geometrical characteristics of the burned pixels in the near-infrared (NIR, 0.87µm) / thermal infrared (TIR, 11 µm) space, while the E1 algorithm is a series of fixed thresholds applied to the data from four spectral channels.

The products were validated against other field and remote sensing data (Simon, 2004). Commission errors were uncommon and affected mostly scattered pixels. The only large area of commission errors is due to older burned areas, in the mixed and evergreen needle leaf forests of Canada and, probably, also in similar ecosystems across Russia. Omission errors were common and very important in some regions, such as the United States (open shrubland and grassland areas), Australia (open shrubland), Zimbabwe (cropland), and Brazil (broadleaf evergreen forests).

3.3.2 GlobCarbon

The European Space Agency GlobCarbon project generated a global monthly 1-km burned-area product, using two regional GBA2000 algorithms and the GLOBSCAR algorithms applied to 1-km SPOT VEGETATION and ERS2–ATSR2/ENVISAT AATSR data, respectively. The two GBA2000 algorithms are the IFI algorithm (Ershov and Novik 2001) developed for the Eurasian boreal forest and the Technical University of Lisbon (UTL) algorithm (Silva et al. 2002, 2003) developed for southern Africa. The GLOBSCAR algorithm, applied to ERS2–ATSR2 for 1998–2002 and to ENVISAT AATSR data for 2003–2007, is based on two separate algorithms. The K1 GLOBSCAR algorithm (Piccolini 1998) and the E1 GLOBSCAR algorithm (Eva and Lambin 1998) A first validation of the GLOBCARBON products was performed using 72 Landsat images (Globcarbon, 2007), using linear regression analysis based on hexagonal grids of equal area. Results were very diverse in different ecosystems and algorithms. For the global validation, results varied from mean correlations of 0.34 (Globscar algorithm) to 0.85 (logical combination of two or more algorithms), with a high standard deviation.

3.4 The SPOT VGT-based global burned area products

There is extensive experience with SPOT-VGT data for regional, continental, and global burned area mapping. Here we briefly review methods, results and assessment of the two available global burned area products developed using SPOT-VGT imagery.

3.4.1 GBA2000

The GBA2000 project relied on SPOT-VEGETATION data to estimate global burned area at 1 km spatial resolution, during the year 2000. Tansey et al. (2004) reported estimates of BA size and number for four broad vegetation classes and at country level. They mapped over 3.5 million km^2 of burned areas, approximately 80% of which occurred in shrublands and woodlands. About 17% of the burned area affected grasslands and croplands, and 3% occurred in forests. Almost 600,000 individual BA were mapped.

The GBA2000 project was based on an international network of partners for the development and testing of a series of regional algorithms and for the production of continental/regional burned area maps. Different methods were considered necessary to deal with specificities of the burned area remotely sensed signal throughout the major biomes of the World (e.g., boreal forest, tropical forest, grasslands). The various continental/regional maps were subsequently patched together, to form a global product. A total of 11 regional algorithms were developed from temporal and spatial subsets of VGT S1 data. In general, algorithms were applied on multitemporal composited data, using a change detection approach. Data classification approaches used included multiple logistic regression, Multi-Layer Perceptron (MLP) neural networks, expectation-based BRDF model inversion, classification and regression trees, and linear discriminant analysis.

Although global validation of the GBA2000 product was not performed, Tansey et al. (2004) mention problems detecting sub-pixel burned areas (a significant problem in regions of tropical forest), mapping burns in cloudy regions, and the false detection of burned areas caused by flooding or dark soils.

3.4.2 L3JRC

The L3JRC project was developed under a partnership between the EC Joint Research Centre (JRC), the University of Leicester, the University of Louvain-la-Neuve, and the Tropical Research Institute, Lisbon. Global burned area maps, at 1km spatial resolution were developed for seven fire years (2000 to 2007), using a modified version of a Global Burned Area (GBA) 2000 algorithm. The total area burned each year (2000–2007) was estimated to range from 3.5×10^6 km^2 to 4.5×10^6 km^2. Validation was based on 72 Landsat TM scenes, and correlation statistics between TM and VGT estimated burned areas were reported for major vegetation types. Accuracy of the global data set was found to depend substantially on vegetation type (Tansey et al. 2008).

The main processing L3JRC algorithm uses a temporal index in the 0.83 μm channel of VGT. This index, I, is computed as:

$$I = (S1_{NIR} - IC_{NIR}) / (S1_{NIR} + IC_{NIR})$$

where $S1_{NIR}$ is the pixel value of the NIR band of the S1 daily product and IC_{NIR} an intermediate composite product. The intermediate composite consists of averaged NIR reflectance derived from all observations prior to observation on the day being considered. No calculation or detection is performed where $S1_{NIR}$ or IC_{NIR} equals zero. Mean and standard deviation values are computed for the index I over a spatially roving window. A pixel is flagged as burned if the pixel value in the roving window, I, is lower than the mean value minus two standard deviations. Two further checks are made on reflectance values in the 0.83 μm (S1 pixel value < 260) and 1.66 μm (S1 pixel value > 250) channels to confirm the burned area (Tansey et al. 2008).

A first validation of the L3JRC burned area product was based on 72 Landsat TM scenes. Estimated accuracy extremely varied from one land cover to the other, with values as low as 3% for mosaic of land covers and maximum values of 56% in herbaceous cover (both in terms of regression slope: Tansey et al. 2008). Accuracy also changed with latitude-ecosystem, with good performances for boreal forest and

much lower in semi-arid Australia and Africa. Under detection by L3JRC seems to be more significant in areas of shrubs and grasses rather than forests. As the original GBA2000 algorithm that was modified for L3JRC had been developed for detecting boreal forest burns, this might be expected. The L3JRC algorithm also underestimates burned area over cultivated and managed lands, possibly because their size is too small for detection by SPOT VEGETATION (Tansey et al. 2008).

3.5 MERIS-based burned area studies

MERIS was primarily designed to provide quantitative ocean-colour measurements (Rast et al. 1999). However, its spectral characteristics make it appropriate to also serve applications like land surface and atmospheric characterisation (see (Calado et al. 2011). It is well known that one of the major drawbacks of MERIS images, for BA identification, is the lack of SWIR bands, which has proven to be crucial to discriminate burned surfaces from water and non-combustible land cover. On the other hand, its multi-spectral imaging capabilities in the VIS/NIR region of the spectrum, moderate spatial resolution and 3 day repeat cycle, may in part circumvent this limitation. In fact, MERIS bands are so narrow that it is possible to detect absorption bands and estimate its depth. Moreover, the sensor was especially designed to detect chlorophyll concentration having though bands in the red edge (bands located in the maximum of chlorophyll absorption). Such bands allow the use of indices of chlorophyll concentration, that may be of use for BA detection, since an abrupt decrease in the chlorophyll content may be related to a fire.

Regarding fire applications, very few studies have been conducted using MERIS instrument. Among the existing studies, there is one developed by Huang and Siegert (2004), where Level 1b MERIS RR product was used to identify plumes and the BA detection was achieved combining night-time AATSR fire hot spots with BA detected with Advanced Synthetic Aperture Radar (ASAR). Another study concerning the estimation of fire severity using MERIS FR Level 2 imagery and MODIS daily reflectivity product (MOD09GHK) was conducted by Roldán-Zamarrón et al. (2006). The BA mapping was performed applying the matched filtering method (Boardman et al. 1995) to Landsat TM data and the fire severity levels were then estimated through use of different techniques to MERIS and MODIS images. The authors concluded that, in general, the fire severity estimation performed by MERIS was more accurate than the one performed by MODIS. Gonzaléz-Alonso et al. (2007) also applied the same technique to MERIS FR Level 1b imagery to estimate fire severity levels and BA at a local scale. Validation was then performed comparing obtained results with the ones obtained using SPOT-5, showing a fairly high correlation between both sensors. Aiming to evaluate the ability of some sensors on the estimation of fire severity levels, Chuvieco et al. (2007) performed a comparative study using SPOT-5, Landsat TM, MERIS and MODIS and concluded that Landsat TM was the one presenting the best performance. Nevertheless, MERIS proved to be capable of correctly identify the spatial pattern of the distribution of the severity levels.

It is worth noting that the above studies are not specifically oriented to burn area mapping, but rather to the analysis of some aspects related to level of damage caused by fires.

Only two works have been found in literature in relation to burned area mapping. The first one used Spectral Angle Images (SAI) technique at a regional scale (Oliva and Martín 2007; Oliva et al. 2010). The SAI methodology makes use of a reference spectrum (endmembers) that in present case was obtained from the image (SAI-image) and from the field spectral measurements (SAI-field). The study used MERIS FR Level 2 images and compared BA discrimination using traditional vegetation indices (e.g., BAI, GEMI, η, NDVI) with SAI technique and validation was carried out using AWiFS images. Obtained results showed that index η (a component of the GEMI calculation) and the SAI-image were the ones that presented higher accuracy. According to the authors, NIR bands in the red edge (bands 9 to 12) region present a higher power of burned area discrimination than NIR bands (bands 13 to 15) in the spectral region traditionally used by the sensors designed for Earth observation (Oliva 2009). From these ones, when using only one post-fire image, band 10 (in the spectral range 750 nm – 757.5 nm) is the one with the highest discrimination power, even though all NIR bands (from band 10 to band 14) present similar discrimination power. On the other hand, when using spectral indices for purposes of burned pixels detection, band 10 in the red edge and band 8 in the red region, were the ones with highest discrimination power. The second study was conducted by González-Alonso et al. (2009). It used MERIS FR Level 1b data for burned land discrimination at a regional scale. The method used in a

synergetic way fire hotspots from MODIS with NIR reflectance values from MODIS and MERIS imagery. Basically, the algorithm consisted in finding the threshold that maximizes the agreement between the burned area discriminated using the NIR band of a post-fire image and the existence of an active fire as detected by MODIS. Again validation was performed using an image from AWiFS and obtained results were very similar when using MODIS and MERIS reflectance values, although slightly better in the case of MERIS. It is worth mentioning that these studies have only been applied to the North-western part of the Iberian Peninsula to the summer of 2006 and to the Province of Heilongiang in the North of China, in the framework of the ESA DRAGON-2 project (González-Alonso et al. 2009).

While studies performed at regional scale show the potential of this sensor to detect burned areas, especially when using hybrid algorithms, to date MERIS has not been used to obtain a global burned area product.

3.6 Conclusions

Both (A)ATSR-based burned area products result from the global application of pre-existing regional algorithms. Classification accuracy was very variable regionally, and relatively low at the global scale. The VGT-based GBA2000 product was developed combining a large number of regional algorithms, with undesirable effects on global consistency. No global accuracy assessment was performed for this product. The L3JRC product, also derived from VGT data, relied on a modified version of a GBA2000 algorithm developed for the Eurasian boreal region, applied at global scale. Burned area classification accuracy was also found to vary substantially with land cover type and was low globally.

There is no previous experience with the use of MERIS data for global burned area mapping, and even regional scale research is very scarce.

Burned area products developed under the scope of the present project are meant to overcome the main methodological limitations of previous work. They rely on new algorithms, designed with data from ten regional study sites covering all major Earth biomes with moderate to high fire incidence. The VGT and (A)ATSR products were developed from a single algorithm applied at global scale, with minor modifications to accommodate specifically distinct features of each sensor. The MERIS-based product also results from the application of a single, global scope algorithm. Although newly designed, VGT, (A)ATSR, and MERIS algorithms incorporate previously developed data, techniques, and concepts for burned area mapping.

4 (A)ATSR, SPOT Vegetation and MERIS algorithms

4.1 Introduction

The perceived main methodological limitations behind the available (A)ATSR-based and VGT-based products are the global application of regional algorithms, the creation of global products "mosaicked" from a multiplicity of regional algorithms, and the simplistic nature of some algorithms used, all of these contributing towards relatively low classification accuracy. Our goal is to develop a single algorithm, robust enough for global application with both sensors, with minor modifications. For MERIS, given the lack of global-scale burned area algorithms/products based on data from this sensor, no similar analysis can be performed, and the algorithm evolves from previous experience at regional scale.

The VGT / (A)ATSR algorithm relies on a single-channel time series change detection approach, complemented with fire seasonality weighting, and spatial-temporal contextual revision of single pixel burned area classification. The time series change detection component of the algorithm has similarities with the algorithms of Govaerts et al. (2002) and Roy et al. (2002). The MERIS algorithm follows a hybrid approach to obtain burned areas on a global scale. It uses temporal composites of individual channels and spectral indices, combined with active fires and a region growing procedure, to detect and map burned areas. The algorithm incorporates concepts from previous hybrid approaches combining the reflective and the thermal signal associated with vegetation burning (Fraser et al. 2000; Giglio et al. 2009; Roy et al. 1999), especially those based on MERIS imagery (González-Alonso and Merino de Miguel 2009; González-Alonso et al. 2010).

4.2 (A)ATSR and SPOT Vegetation detailed algorithm descriptions

The algorithm for mapping burned areas using SPOT-VEGETATION and (A)ATSR imagery relies on spectral, temporal, and spatial data. More precisely, it looks for spatial and temporal patterns in spectral data that indicate vegetation burning. We analyse single channel (near infrared, NIR) time series of surface reflectance data, which were previously screened for clouds, smoke and haze. Permanent and temporary water bodies were also masked out of the dataset (Bachmann et al. 2014).

The algorithm is designed to answer a series of questions:

   a) Was there a spectral change, at a given date? (change point detection)
   b) Does it look like burning and does it happen at a plausible date? (selecting and scoring change points)
   c) Is there evidence of burning in that neighbourhood, that day and during previous days? (Markov Random Field segmentation)

The first three questions are addressed analysing time series of data at the level of a single pixel, while answering the last question requires taking into account the information contained in areas defined by a variable number of pixels. Question a), estimating the point in time at which the statistical properties of a series of NIR surface reflectance data have changed, is addressed with a Change Point Detection (CPD) technique. Once potentially multiple change points have been identified, question b) is answered by scoring each change point based on its date of occurrence, and spectral characteristics related to the NIR reflectance change associated with it, both in time and in space. Finally, c) revises the initial (a-b) burned area detection and mapping, in the light of evidence of burning in the spatial neighbourhood of a given pixel, during the day it was detected and also during a short preceding period, yielding the final burned area map. Figure 3 illustrates the algorithm.
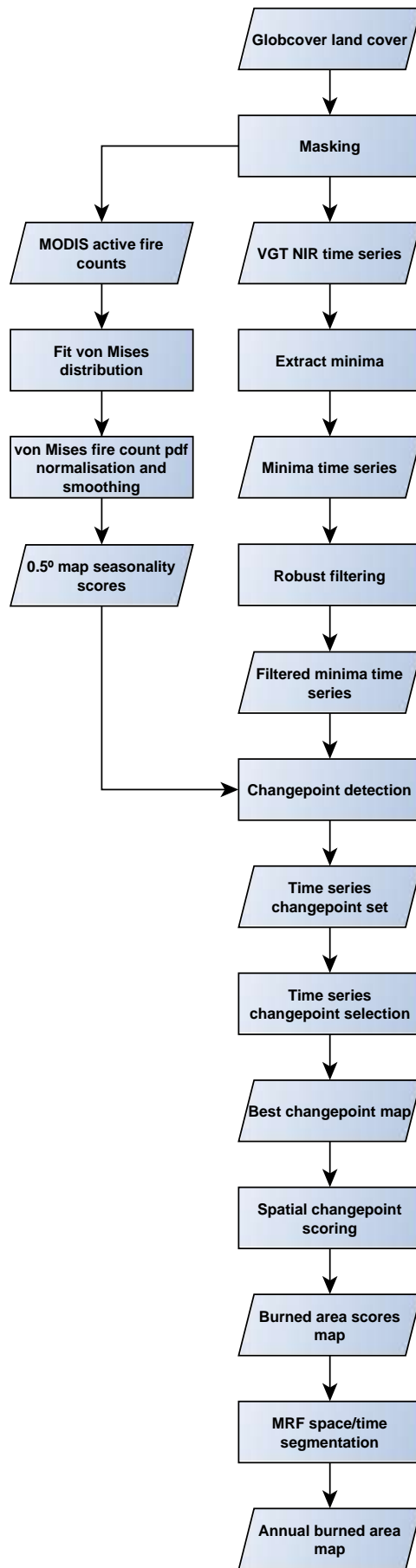
Figure 3: SPOT-VGT / (A)ATSR burned area classification and mapping algorithm

4.2.1 Change detection algorithm

4.2.1.1 Time series pre-processing

The pre-processed surface reflectance time series display an oscillating pattern caused by variations in illumination and observation geometry, the bidirectional reflectance distribution function (BRDF) effect, which increases the variability of the data, independently from any actual changes occurring at the land surface. Additionally, the time series also reveal residual atmospheric effects, which generate positive outliers ("spikes") in the data, again unrelated to land surface changes. The signal we are trying to detect, vegetation burning, appears as a decrease in values of the NIR surface reflectance time series. Although this decrease often is evident in both the maximum and the minimum of each BRDF-induced oscillation, it tends to be more consistently and reliably expressed in the minima values, which are least affected by residual atmospheric contamination. Therefore, we extract a time series of minima from the original NIR surface reflectance data. These time series also contain negative outliers, usually caused by cloud shadowing, and occasionally due to unscreened flooding, corresponding to pixels that were not captured by the screening procedures described in Bachmann et al. (2014). Robust filtering of the time series of surface reflectance minima is therefore applied to remove most of these negative outliers, yielding time series suitable for CPD. The time series pre-processing step of the algorithm was used only with the SPOT-VGT data. The (A)ATSR lower frequency of observation yields time series without enough data for the pre-processing step to work properly. However, (A)ATSR data are substantially less affected by BRDF effects, and thus are appropriate for immediate application of changepoint detection.

4.2.1.1.1 Extraction of local minima

Extracting local minima from a time series of observations $y_{1:n} = (y_1, \ldots, y_n)$ of reflectance data entails a series of steps:

1. Identification of "turning points". An observation y_i is a turning point, i.e. a local minimum, y_{t_m}, (local maximum, y_{t_M}), if its two neighbours are both smaller (larger) (Kugiumtzis and Tsimpiris, 2010).
2. Remove from the series all y_i that are not turning points.
3. Calculate a time series of first-order differences and remove all turning points that differ from one of its immediate neighbours less than 0.02 reflectance units, i.e. points associated with minor, spurious oscillations in the series. Parameter min_diff_cutoff , δ_{min}.
4. Remove all remaining local maxima, y_{t_M}. After this step, then remaining points are shown in red in Figure 4.
5. Remove those $y_{t_m} \geq 0.4$ reflectance units, which are considered contaminated by residual atmospheric effects. Parameter max_refl_cutoff, ρ_{max}.

The values for the min_diff_cutoff and max_refl_cutoff parameters were estimated empirically, from the quantitative analysis of a large number of single pixel time series, from the ten study sites available for algorithm development.
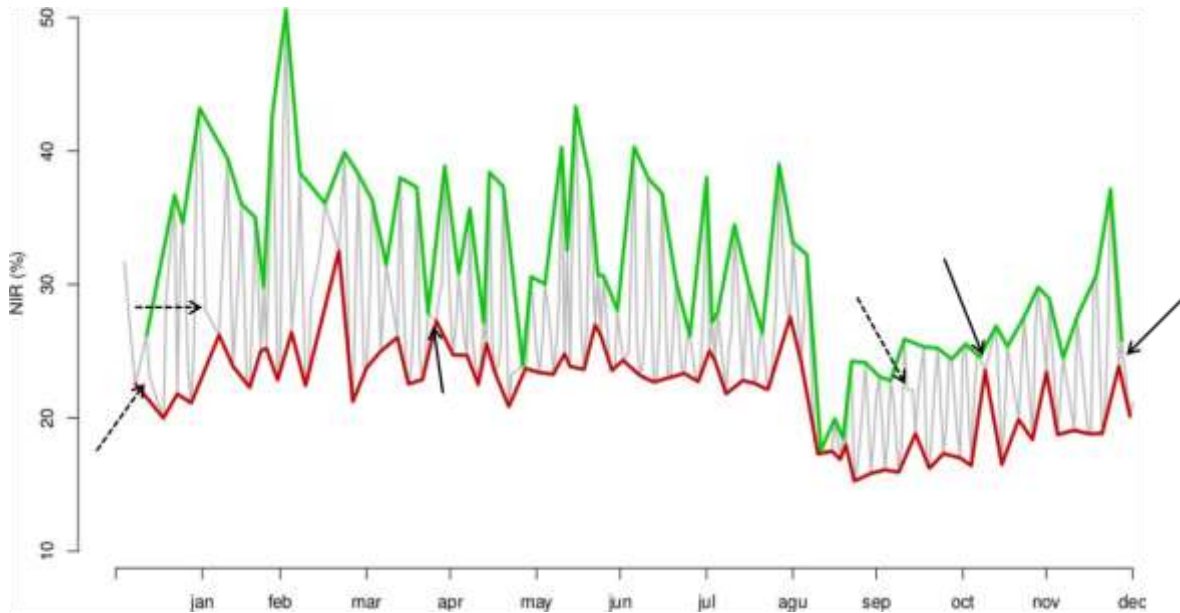
Figure 4: Original SPOT-VEGETATION time series (grey) for a single pixel over one full year. Turning points are shown in green (maxima) and red (minima). Dashed arrows show examples of non-turning points and solid arrows show spurious oscillations, which generate positive outliers in the time series of minima.

The resulting series of local minima (Figure 4) may contain outliers ("spikes"), which may be positive when generated by spurious oscillations that exceed δ_{min}, or negative, mainly due to cloud shadow.

4.2.1.1.2 Robust filtering

Several of the time series of NIR reflectance for the study sitesof NIR reflectance minima show outliers (Figure 5), most of which correspond to a single date, although patches of two or three consecutive outliers may occur. These mostly negative "spikes", although spectrally similar to burns, display much shorter persistence. The time series display periods of relative stability, slow monotonic trends, sudden level shifts and environmental and measurement artefacts. Such data require a method that performs fast and reliable noise removal, distinguishing extraneous effects from spectrally relevant changes at the land surface. The filtering approach of Fried (2004) uses robust regression for local approximation of the trend in a moving time window and replaces outliers based on robust scale estimators. Gather and Fried (2004) provide rules for automatic choice of window width, using the regression residuals. Implementation of this robust filtering approach in the "R"software suite (Fried et al. 2011, http://cran.r-project.org/web/packages/robfilter/robfilter.pdf) requires the specification of a series of parameters for model fitting, local variability (scale) estimation, and outlier detection and handling:

- Robust Trend Approximation (*trend*) refers to the method used to approximate the signal within one time window. Set to *repeated median regression* (RM).
- Initial window width (*width*) is a positive integer defining the initial window width used for robust regression fitting. Set to a width of *3*.
- Scale estimate (*scale*) is the method used for robust estimation of the local variability (within one time window). Set to Rousseeuw's and Croux' (1993) Qn scale estimator (QN)
- Outlier Detection (*outlier*) specifies the rule to be used for outlier detection and outlier treatment. Observations deviating more than $d.\hat{\sigma}_t$ from the current level approximation $\hat{\mu}_t$ are replaced by $\hat{\mu}_t \pm \kappa \hat{\sigma}_t$ where $\hat{\sigma}_t$ denotes the current *scale* estimate. Set to

winsorization (*W*) approach, which limits extreme values in the data to reduce the effect of possibly spurious outliers, by shrinking large and moderately sized outliers (*d* = 2) towards the current level estimate (*k* = 2).

- Shift detection (*shiftd*) is the factor by which the current scale estimate is multiplied for shift detection. Set to *2σ*.
- Maximal window width *(max.width)* a positive integer (>= *width*) specifying the maximal width of the time window. Set to *7*.
- Window width adaptation *(adapt)* is the moving window width adaptation parameter. *adapt* can be either 0 or a value ∈ [0.6; 1] . *adapt* = 0 means that a fixed window width is used. Otherwise, *max.width* is reduced whenever more than a fraction ∈ [0.6; 1] of the residuals in a certain part of the current time window are all positive or all negative. Set to *0.8*.
- *Extrapolate* defines the rule for data extrapolation to the edges of the time series. As implemented, it consists of the fitted values within the first half of the first window and within the last half of the last window.
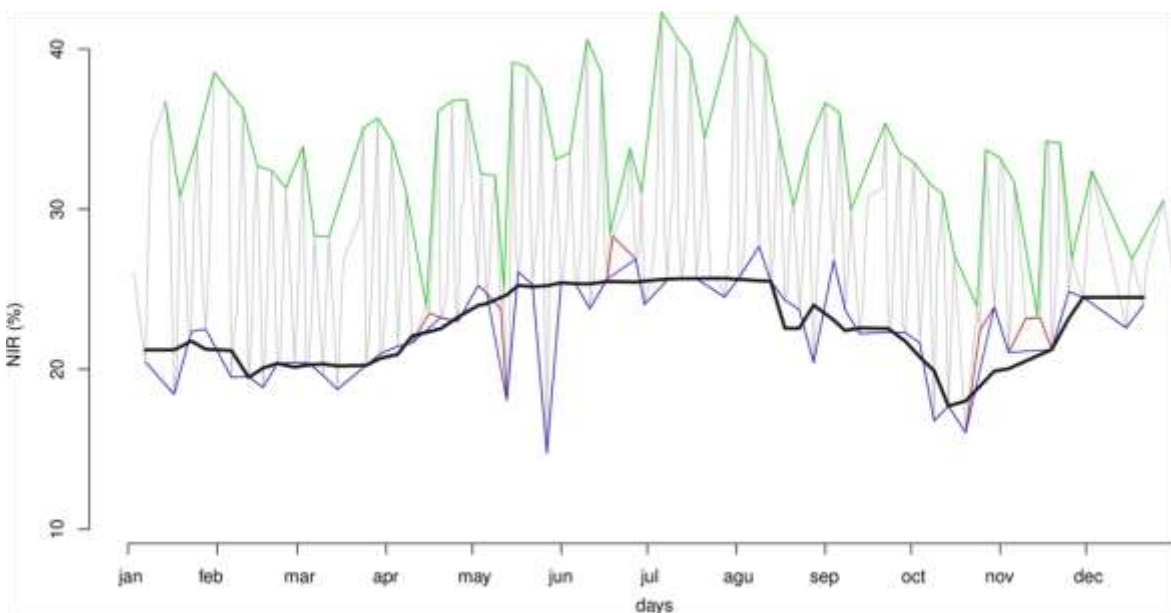
Figure 5: SPOT-VEGETATION time series (grey) for a single pixel over one full year. Turning points are shown in green (maxima) and red (minima). Blue line shows time series of minima without high values produced by spurious oscillations. Black line shows time series of minima with spikes removed by robust filtering.

4.2.1.2 Changepoint Detection

We adopt the approach of detecting changepoints in a time series through minimizing a cost function over possible numbers and locations of changepoints. The approach relies on a new method for finding the minimum of such cost functions, and hence the optimal number and location of changepoints, which has a computational cost that is linear in the number of observations (Killick et al., 2012). Changepoint detection within a time series consists of two steps: i) choice of statistical criteria to optimise and ii) optimisation algorithm. PELT is an algorithm for the optimisation step that can implement many choices of criteria including likelihoods. Common algorithms for the optimisation step include Dynamic Programming (Auger and Lawrence, 1989) and Hidden Markov Models (Chib,1998) which produce exact optimisations but are computationally slow, O(n2); and Binary Segmentation (Scott and Knott, 1974) and Genetic algorithms (Jong et al., 2004) which are computationally fast, O(n log n) but produce approximate optimisations. In contrast PELT, which is an algorithm for the optimisation step that can implement many choices of criteria including likelihoods (Killick et al. 2012), was chosen because it is computationally fast (O(n)) and produces an exact optimisation.

4.2.1.2.1 Pruned Exact Linear Time (PELT) algorithm

The Pruned Exact Linear Time (PELT) algorithm proposed by Killick et al. (2012) produces exact optimisation of changepoint segmentations in linear computational time. This is achieved using dynamic programming (computational time to $O(n^2)$) and pruning to further reduce the computational time to $O(n)$. For a given point n in a sequence, determining the optimal segmentation of the data prior to n with an unknown number of segments requires consideration of 2^{n-1} solutions. Dynamic programming techniques can be implemented to reduce the problem to simply consider the last change prior to n. Thus, at a given point n, the solution is simply which of the $n-1$ previous locations is the last changepoint prior to n. The number of options scales linearly with n and thus the computational time is $O(n^2)$. The PELT algorithm extends this idea further. The intuition behind the algorithm is that once an `obvious' change is encountered, say at $n - 5$, then data points before this, e.g. $n–6, n–7,…,$ will never be the last change prior to $n$. Killick et al. (2012) quantify `obvious' with a bound which ensures that the algorithm remains an exact optimisation. Furthermore, when a likelihood is used as the criterion to optimise, Killick et al. (2012) prove that, under regularity conditions, the computational cost of PELT is $O(n)$. A mathematical description of PELT is given in Table 1 and the method is available in the "R" programming language (Crawley, 2007) package *changepoint* (Killick and Eckley, 2010).

Table 1: PELT algorithm for identifying multiple changepoints.

Input:	A time series of the form $(y_1, y_2,…, y_n)$ where $y_i \in$ R.
	A measure of fit $C(.)$ dependent on the data.
	A penalty β independent of the number and locations of changepoints
Initialise:	Let n = length of time series
	Set F(0) = -β, cp(0) = 0, p=0.
Iterate:	For $\tau^* = 1, …, n$
	1. Calculate $F(\tau^*) = \min_{\tau \in (0, p, \tau^*-1)} \left[F(\tau) + C(y_{(\tau+1):\tau^*}) + \beta \right]$.
	2. Let $\tau^1 = \arg\{ \min_{0 \le \tau < \tau^*} \left[F(\tau) + C(y_{(\tau+1):\tau^*}) + \beta \right]$
	3. Set $cp(\tau^*) = \left[cp(\tau^1), \tau^1 \right]$.
	4. Set $p = \arg_r \{ F(\tau) + C(y_{(\tau+1):\tau^*}) + \beta + K > F(\tau^*) + \beta \}$.
Output:	The changepoints recorded in *cp(n)*.

4.2.1.2.2 Detecting changes in mean

The PELT algorithm can be implemented with many optimisation criteria. In this work we seek to identify changes in mean within NIR reflectance data (Figure 6). We assume that the NIR reflectance follows a Normal distribution with a constant variance and changing mean. Following Hinkley (1970), the optimisation criteria ($C(.)$ above) based on the likelihood is

$$C(y_{(\tau_i+1):\tau_{i+1}}) = \sum_{j=\tau_i+1}^{\tau_{i+1}} y_j^2 - \frac{(\sum_{j=\tau_i+1}^{\tau_{i+1}} y_j)}{\tau_{i+1} - \tau_i}$$

(1)

Within PELT, we used the Schwarz Information Criterion (SIC; Schwarz, 1978) as the penalty function to penalise against identifying too many changepoints, because the larger penalty term in SIC, compared to the more commonly used Akaïke Information Criterion (AIC), performed better in terms of avoiding an excessive number of change points being detected. This method is implemented using the multiple.mean.norm function in the "R" software environment (Killick and Eckley, 2010). The time series data are not strictly normal, but the method is robust to moderate violations of this assumption.
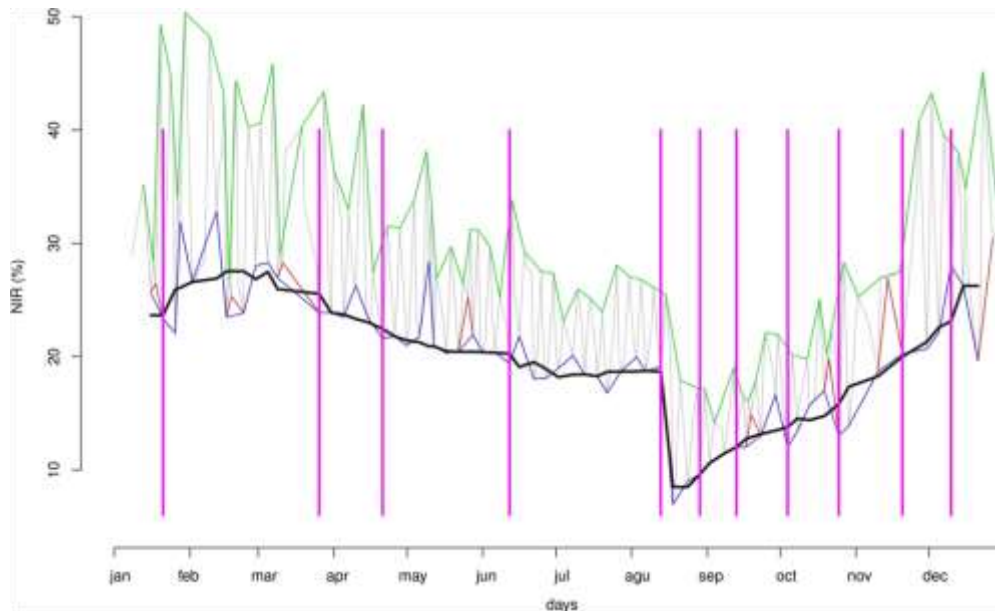

Figure 6: Changepoints (vertical purple bars) detected on the time series of filtered minima (black line), using the PELT algorithm, with SIC penalty function

4.2.1.3   Changepoint selection and scoring

The PELT/SIC approach to CPD may yield several changepoints per pixel / time series, and per season, since the mean value of NIR reflectance data varies not only in response to burning, but also as a function of cyclic weather patterns, atmospheric conditions, vegetation phenology and anthropogenic land cover changes. Therefore, it is necessary to select the changepoint most likely to correspond to the identification of a burning event in each pixel / time series. In order to be considered as candidates for scoring, changepoints need to satisfy all of the following criteria:

a)   The CP must be associated with a decrease in NIR reflectance($\overline{S_{i+1}} - \overline{S_i}$:<0).

b)   The NIR reflectance decrease must not exceed 0.2 reflectance units ($\overline{S_{i+1}} - \overline{S_i}$:<0.2).. Larger decreases typically are associated with cloud contaminated data in the segment preceding the CP.

c)   The post CP NIR reflectance must be smaller than 0.2 reflectance units ($\overline{S_{i+1}}$ <0.2). Higher reflectance values typically are not associated with fire-affected surfaces.

d)   The CP requires a temporal density of 0.1 in the pre-CP segment, i.e. at least one valid observation per each 10 days of time series segment duration

e)   The CP requires a temporal density of 0.1 in the post-CP segment

f)   It requires that the reflectance value of a CP is smaller than the sum of lowest reflectance value in the post-CP segment plus 0.005 reflectance units.

g)   The slope of a linear fit to the NIR reflectance time series data in a post-CP segment cannot exceed 0.4. Higher rates of post-CP NIR reflectance recovery are inconsistent with post-fire vegetation recovery.

h) The dates of the CP with the two lowest NIR reflectance values in the time series cannot be separated in time by a period longer than half of the duration of the time series. Included to prevent selecting CP associated with the decreasing phase of NIR reflectance in time series with strong vegetation seasonality.

i) The CP requires a minimum of three valid time series observations before (after) the first (last) CP in the time series for the NIR reflectance change measurement to be considered reliable.

Next, the changepoints fulfilling these criteria are scored against a set of ideal points, representing the most paradigmatic regional examples of burned areas, in terms of NIR reflectance change, post-fire NIR, and timing of the fire. Compromise programming is the technique chosen to perform temporal changepoint selection and spatial changepoint scoring.

4.2.1.3.1 Compromise programming

Compromise programming (CP), is a multi-criteria decision analysis (MCDA) technique appropriate for use in a continuous multiple objective context (Zeleny, 1973), modified for the analysis of discrete problems by Duckstein and Opricovic (1980). This method identifies the alternatives which are closest to an ideal point, as determined by some measure of distance. Compromise programming is used at two stages in the (A)ATSR / VGT burned area mapping algorithm: first, to select the changepoint from each time series/pixel most likely to correspond to a burning event; second, to score each pixel in the selected changepoint annual map for each tile (or study site) in terms of its likelihood of representing a burning event. The latter scores are input for the Markov Random Field spatial/temporal BA classification revision procedure, the last step in the algorithm.

The set of initial feasible alternatives to be evaluated (e.g. the set of all changepoints in a single-pixel time series) is (Zeleny, 1982, pp. 154-155):

$$X = \{x^1, x^2, \dots, x^m\} \qquad (1)$$

and each changepoint is characterized by n attributes, or criteria. The kth changepoint can be written as:

$$x^k = (x_1^k, x_2^k, \dots, x_n^k) \quad k = 1, 1, \ m \qquad (2)$$

Individual x_i^k designate the level of attribute i attained by changepoint k, where $i = 1, \dots, n; \quad k = 1, \dots, m$. Therefore, x^k is a vector of K numbers, assigned to each changepoint and synthesizing all available information about it and defining a multiple criteria alternative (Zeleny 1982, p. 155). If we now consider the ith individual evaluation criterion, the set X produces a vector with K numbers:

$$x_i = (x_i^1, \dots, x_i^K) \qquad (3)$$

This vector represents all currently attained levels of the ith attribute, for example, the NIR spectral reflectance changes $(\overline{S_{i+1}} - \overline{S_i})$ associated with each changepoint. From among these values or levels, there is at least one ideal value that is preferred to all others, and the concept generalizes to the multiple criteria alternative as the set of all individual ideal levels, or *ideal point*, denoted as:

$$x^* = (x_1^*, x_2^*, \dots, x_n^*) \qquad (4)$$

The vector **x*** represents the ideal point, a usually unavailable alternative, characterized by displaying the best attainable score on every criterion. Using compromise programming, all available changepoints are rated based on their multidimensional distance to the ideal point, according to a chosen distance metric. A generalized family of distance metrics (Minkowski), dependent on the exponent *p*, can be expressed as (Zeleny, 1982, p. 317):

$$L_p\left(\lambda, k\right) = \left[\sum_{i=1}^{n} \lambda_i^p \left(1 - d_i^k\right)^p\right]^{\frac{1}{p}} \qquad (5)$$

where $\lambda = \left(\lambda_1, \dots, \lambda_n\right)$ is a vector of attribute weights, λ_i ($\lambda_i > 0$ and $\sum \lambda_i = 1$) and *p* is the distance parameter ($1 \leq p \leq \infty$). Varying *p* affects the relative contribution of individual deviations from the ideal point, a greater emphasis being given to larger deviations as *p* tends towards ∞. A value of *p* = 2, corresponding to an Euclidian distance metric, was chosen for implementation in the (A)ATSR/VGT burned area mapping algorithm.

The abovementioned data normalization to a [0, 1] range was accomplished using the eqs. 6 and 7, where x_i^* and x_{i*} are anchor values, respectively the most desirable and the least desirable observed score for criterion *i*:

$$d_i^k = \frac{x_i^k - x_{i*}}{x_i^* - x_{i*}} \qquad (6)$$

when the most preferred score is a maximum (e.g. $\overline{S_{i+1}} - \overline{S_i}$, mean NIR spectral reflectance change associated with a given changepoint), and

$$d_i^k = \frac{x_i^* - x_i^k}{x_i^* - x_{i*}} \qquad (7)$$

when the most preferred score is a minimum (e.g. $\overline{S_{i+1}}$, mean NIR post changepoint spectral reflectance change associated with a given changepoint).

4.2.1.3.2 Selection of changepoints in single-pixel time series

Application of CP at the level of each single-pixel, annual time series is performed with the goal of identifying the changepoint in the time series most likely to coincide with spectral changes induced by a burning event. Changepoints associated with an increase in reflectance and those preceded or succeeded by time segments with low density of observations (< 10% valid days in the segment), are discarded prior to evaluation. Changepoint scoring relies on three attributes, or criteria, *i*:

-   Change between the mean reflectances of the segments succeeding and preceding each changepoint detected in the time series, $\overline{S_{i+1}} - \overline{S_i}$
-   Mean reflectance of the segment succeeding each changepoint, $\overline{S_{i+1}}$
-   Value of the normalised [0,1], spatially smoothed, von Mises probability density function of the 10-day active fire counts in each 0.01° grid cell, defining a fire seasonality score, F_{vM}.

The ideal point for the set of changepoints detected in each single-pixel time series is composed of the largest NIR reflectance change, the lowest succeeding mean reflectance value, and the largest fire seasonality score. It is possible that no changepoint detected in an annual time series corresponds to an actual burning event. Nevertheless, the changepoint closest to the ideal point, under a Euclidean (*p*=2) distance metric will be chosen as the best candidate for inclusion in the annual map.
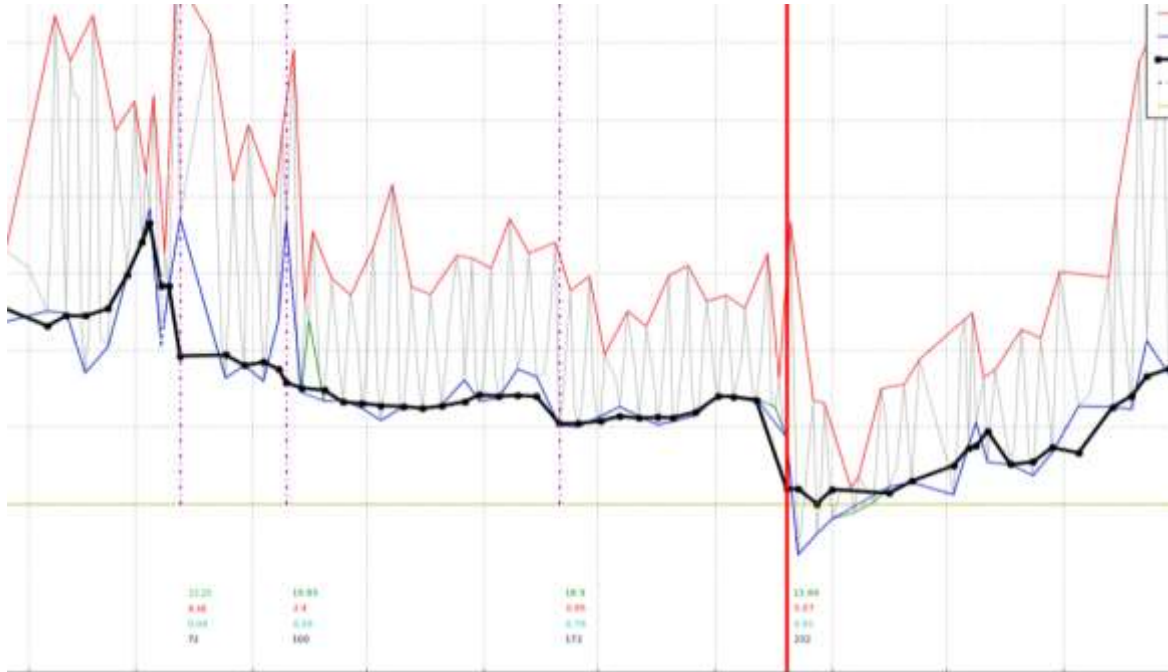

Figure 7: VGT NIR reflectance time series of a pixel in the Australia study site (2005) showing four changepoints detected with PELT

Figure 7 shows VGT NIR reflectance time series of a pixel in the Australia study site (2005), showing four changepoints detected with PELT. The changepoint more likely to represent a burning event is marked with the red vertical line. This point displays neither the largest $\overline{S_{i+1}} - \overline{S_i}$, nor the smallest $\overline{S_{i+1}}$. However, it is the closest to the ideal point in the 3-criteria evaluation space.

4.2.1.3.3 Fire seasonality score

The fire seasonality score is the most complex of the four criteria used in time series changepoint selection. The following describes the rational for its use and how it is derived.

Global vegetation fire displays temporal patterns that are determined by a combination of climatic and anthropogenic factors (Giglio et al. 2006; Le Page et al. 2008, 2010) and typically occur during the local dry season, which varies greatly in duration and timing. The fire season was defined on a 1° grid cell and 10-day composites, using MODIS global monthly active fire location product (MCD14ML, collection 5) for the period 2001 - 2009. The data were previously screened using the approach of Mota et al. (2006) and Oom and Pereira (2013). The total number of active fires detected in each grid cell and time composite over the study period was plotted as a circular histogram and fitted with a mixture of *N* von Mises probability distributions (Fisher, 1995), the analogue of the normal distribution, for circular data. The number of von Mises distributions used varied from 1 to 2 corresponding, to uni- and bimodal distributions, respectively. For each component (j) the probability density function is defined by Eq. 5:

$$vM_j\big(\theta; \kappa_j; \mu_j\big) = \frac{1}{2\pi I_0(\kappa_j)} \exp[\kappa_j \cos(\theta - \mu_j)] , \quad 0 \le \theta < 2\pi \tag{5}$$

where, $\kappa_j \geq 0$ and $0 \leq \mu_j < 2\pi$ are the concentration and mean parameters, respectively. The probability model of the mixture of von Mises distributions mvM(Θ) is given by Eq. 6:

$$mvM(\theta) = \sum_{j=1}^{N} \omega_j vM_j(\theta) \tag{6}$$

where, $0.05 \leq \omega_j \leq 0.95$ is the mixture proportion of each component and $\sum_{j=1}^{N} \omega_j = 1$ (Mardia and Jupp, 2000; Jones, 2006).

The mixture model was optimised by estimating its parameters to obtain the best fit between observed and predicted active fire cumulative frequency (e.g. Carta et al. 2007). In each grid cell, fire counts in each temporal composite were normalised by dividing them into the maximum number of fire counts recorded as a single composite, for scaling between 0 and 1. The single independent variable was the day of the year (recoded in radians). Non-linear curve fitting was performed with the automatic Newton search method, aiming at minimizing the square of absolute differences between observations and estimates (Coleman and Li, 1994). The only constraint applied to the parameter search space was $\kappa_j \geq 0.5$, to avoid fitting uniform distributions (Fisher, 1993) to data without significant fire seasonality.

Model performance was evaluated with the model efficiency index (hereafter, MEF), a measure of model predictive power (Nash and Sutcliffe, 1970). The index was calculated considering the observed and estimated normalised, non-cumulative, fire frequency. For each pixel, the circular mixture model with the highest MEF was selected, regardless of the number of parameters involved, guaranteeing the best possible fit. Cells with MEF < 0.7 were considered poor fits to the data, and no fire season start and end were estimated for these cells. Fire seasonality scores only were determined for cells containing a total of least 270 fire counts over the nine years of data, and with fire observations in at least 2 years. Figure 8 shows the distribution of the best MEF obtained at global scale. About 80% and 70% of the pixels have MEF higher than 0.6 and 0.75, respectively, showing the good overall model fit.
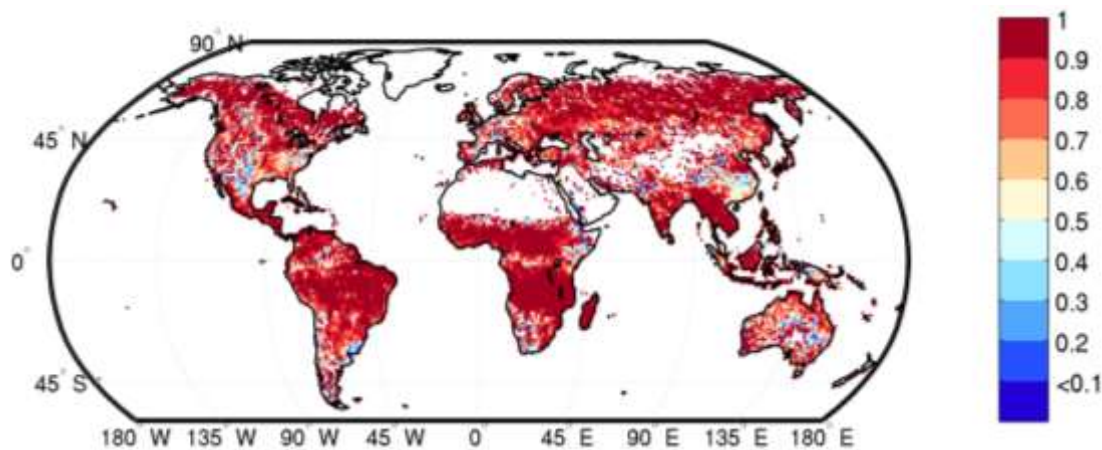

Figure 8: Global MEF distribution of the best fit von Mises (uni- or bimodal) distribution

Figure 9 - Figure 11 show the circular distribution of observed and estimated frequencies for 0.5° cells located in Angola, Kazakhstan, and Indonesia. The seasonal distribution of fire activity was, unimodal and bimodal in Figure 9 and Figure 10. Figure 11 shows data for a cell where the distribution is multimodal, model fit is poor, and no seasonality filter is applied, i.e. the full year is processed.
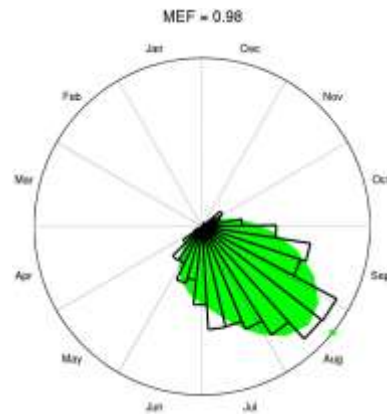
Figure 9: Unimodal von Mises distribution fit to fire frequency data from Angola 0.5^0 grid cell. Fire season is considered to start in mid-May and end in early October. Bars represent fire counts in 10-day composites, the green cloud is the fitted von Mises distribution, and the green dot on circumference is the central date of the fire season.
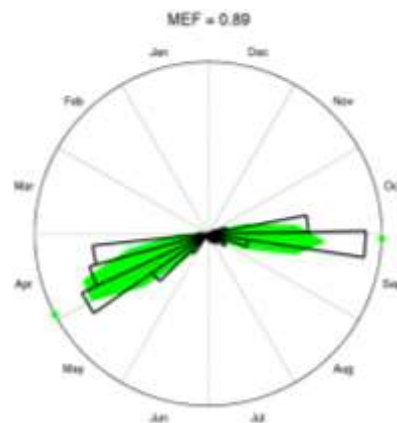

Figure 10: Bimodal von Mises distribution fit to fire frequency data from Kazakhstan 0.5^0 grid cell. Fire season is considered to start in April and end in mid-October. Bars represent fire counts in 10-day composites, the green cloud is the fitted von Mises distribution, and the green dots on the circumference are the central dates of each fire sub-season.

Figure 11: Multimodal von Mises distribution fit to fire frequency data from Indonesia 0.5^0 grid cell. No clear fire season is discernible, in spite of some data concentration in February-April, with secondary modes of activity in June and October. No fire seasonality filter is applied in cases with more than two modes, implying processing data for the full year. Bars represent fire counts in 10-day composites, the green cloud is the fitted von Mises distribution, and the green dots on the cir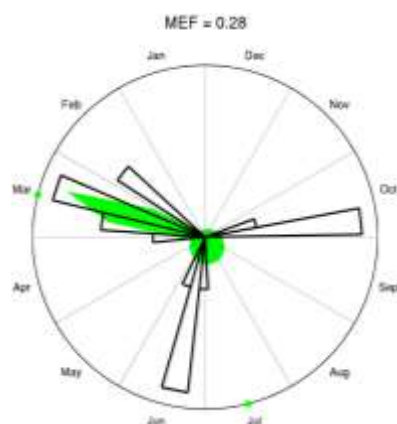cumference are the central dates of each fire sub-season. Distribution fit is poor (low MEF) and central dates are inaccurate.

The von Mises probability density function map was smoothed with a 5 x 5 Gaussian filter, which also filled gaps left by cells that did not satisfy either the model fit or data availability conditions. Figure 12 shows the pdf of a filtered cell, after normalisation to a $0 - 1$ range.
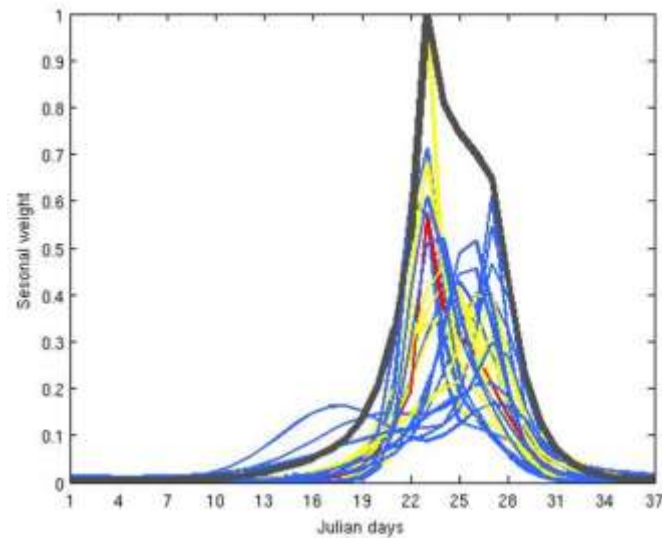

Figure 12: Smoothed, normalized von Mises fire count probability density function (black line). The coloured lines show the contributing pdf contained with the 5 x 5 Gaussian filter kernel.

4.2.1.3.4   Scoring annual changepoint maps

An annual burned area candidate changepoint map is constructed for each global tile, containing three of the layers corresponding to the time series changepoint evaluation criteria. A new ideal point is defined, where the alternatives under evaluation are the changepoints selected out of each pixel/time series, and each pixel is scored in the same way as previously done for the single-pixel annual time series.

Global-scale scoring of the candidate changepoints from each timeseries/pixel relies on the calculation of Euclidean distances to an ideal and to an anti-ideal, which are represented by sets of points, rather than by single points. The ideal set contains one point/site/year from 9 of the 10 project regional study sites (Borneo was excluded due to lack of exemplary cases of burned areas, during the study period), representing the most paradigmatic examples of fire-affected pixels, in terms of non-rescaled values variables mean segment reflectance decrease, the post-change point segment reflectance, and the associated seasonal weight. Definition of ideal points at the scale of each study site/tile contextualizes the scoring procedure, taking into account the global variability in the fire-induced spectral changes that result from heterogeneity in vegetation, meteorological conditions, and land-use. The convex hull of this set of ideal points was determined and distances between the change point selected from each time series/pixel and the ideal set are calculated. The distance to the nearest point in the convex hull is selected (minimum distance) as the distance to the ideal set, according to a mathematical definition of distance between a point and a set of points. Distances to an anti-ideal set were also calculated for each pixel as the shortest of the orthogonal distances to a constant value of 0.02 and 0.2 units, respectively for mean segment reflectance decrease and post-change point segment reflectance (Figure 13,). Changepoints corresponding to a reflectance decrease higher than 0.2 were considered an effect of residual atmospheric contamination, while post changepoint segments with mean reflectance lower than 0.05 typically correspond to unmasked dynamic water bodies. Finally, for each timeseries/pixel, the distances to the ideal (Di_i) and anti-ideal (Dai_i) sets were combined to obtain the p-scores. Figure 13 illustrate the global-scale scoring of the candidate changepoints fot Angola 10° x 10° tile.
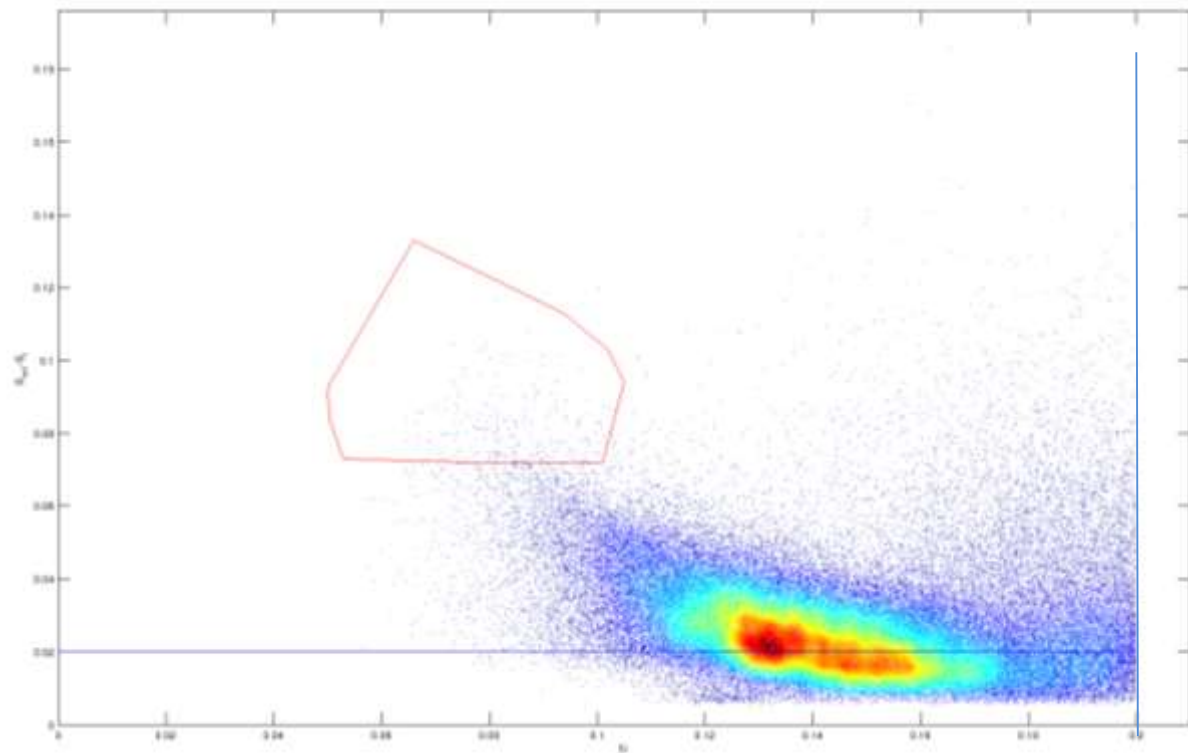
Figure 13: Changepoint density scatterplot from Angola 10° X 10° tile (L10C19). The red polygon represent the convex hull of a set of ideal points. The blue lines represent the constant value anti-ideal levels of 0.02 and 0.2 units, respectively for mean segment reflectance decrease and post-change point segment reflectance

Figure 14 - Figure 18 illustrate the evaluation criteria maps and a distance-to-ideal map for Australia 10° x 10° tile (L10C31) for 2007.

Figure 14: Reflectance decrease map

Figure 15: Post-changepoint segment mean reflectance map

Figure 16: Minimum Euclidean distance to the set of ideal points map

Figure 17: Smallest of the two orthogonal distances to the anti-ideal values

Figure 18: Changepoint score based on reflectance change, post changepoint reflectance and fire seasonality. Higher values (red) are closer to ideal, i.e. more likely to represent burned areas.
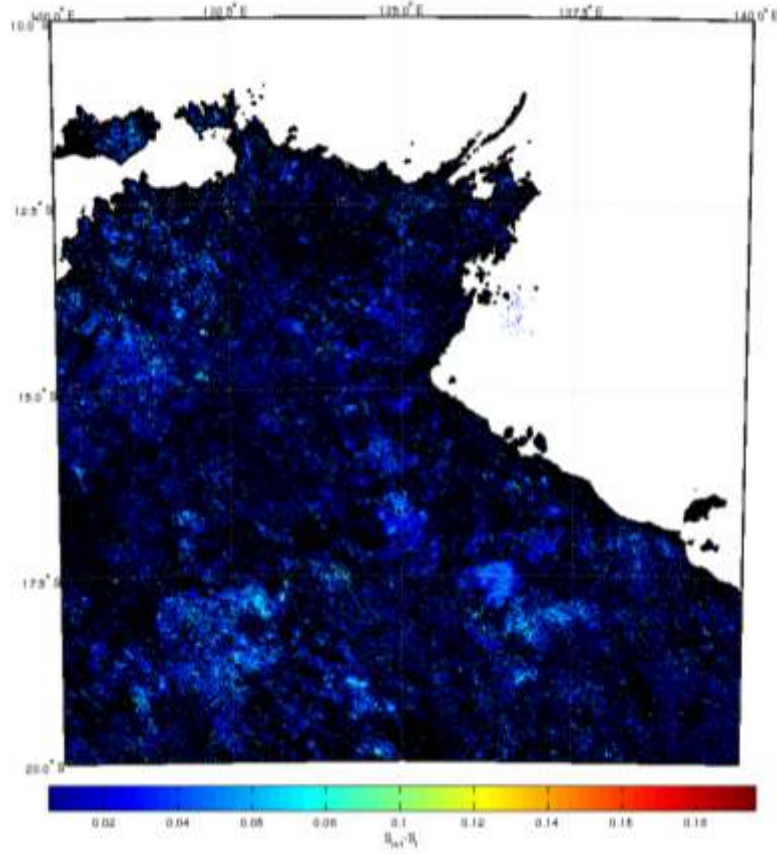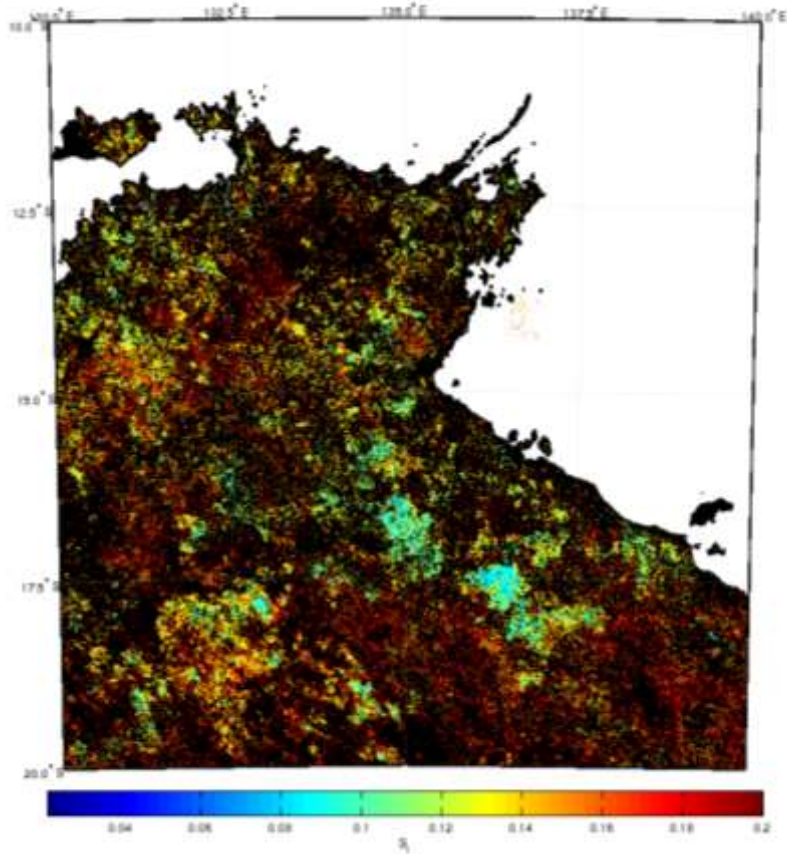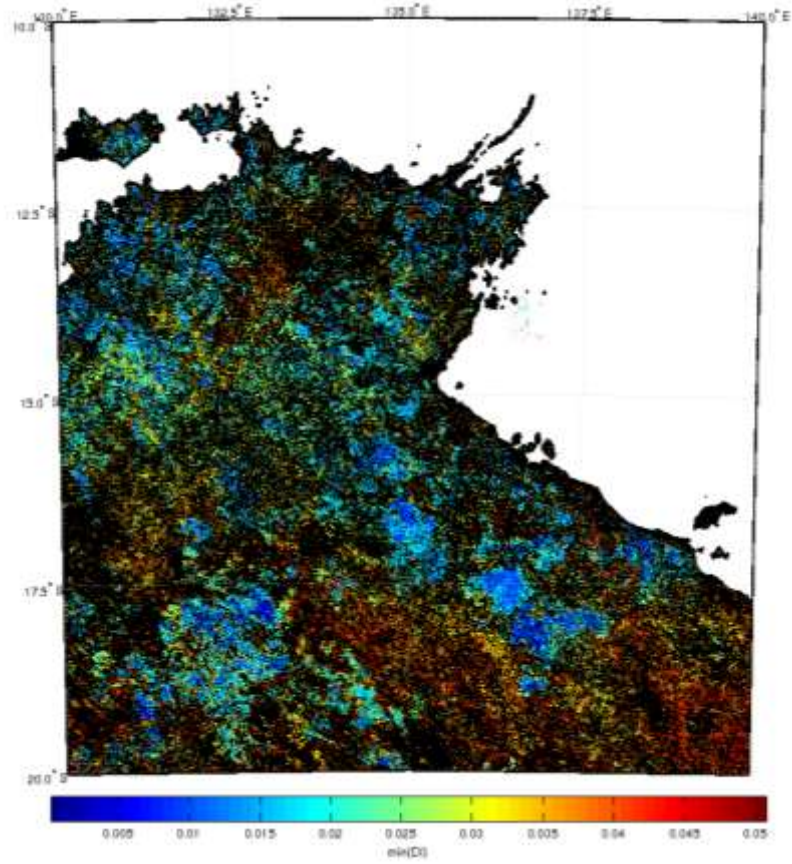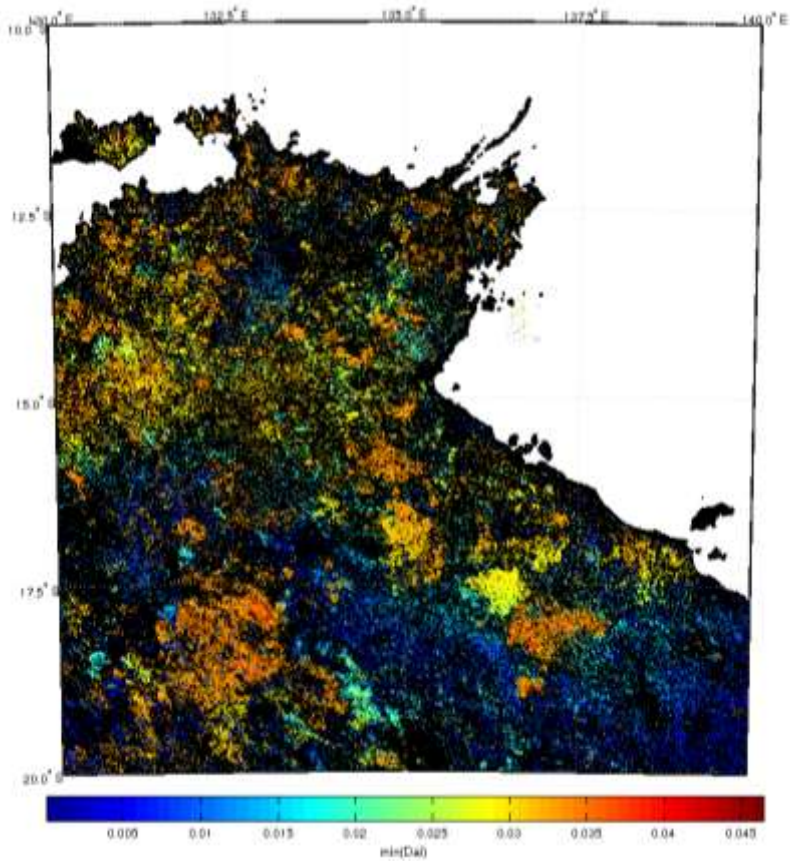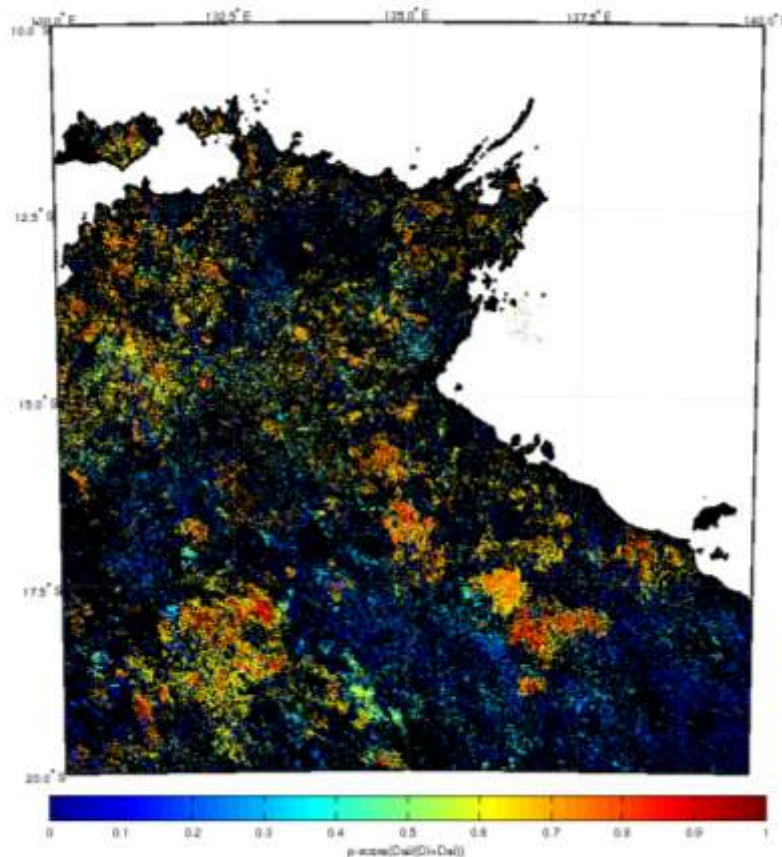
4.2.1.4 Markov random field image segmentation

The pixels with no computed score or detection date are not classified as burned or unburned. The remaining pixels are classified according to the procedure described below.

The previous steps of the algorithm lead to a characterisation of each pixel of the image through two variables: score and detection date. The rationale behind this last processing step is to establish a global classification of the pixels of the image taking into account the spatial relations between pixels and the time relations between dates of detection. The algorithm is a standard image processing algorithm that solves the maximum a posteriori – Markov random field (MAP-MRF) problem, which arises in image segmentation or image restoration.

4.2.1.4.1 Parameters

To define the graph from the score and date of detection values we first need to establish the spatial neighbourhood for each pixel (e.g. 4 or 8 neighbours) and we need to set four parameters: min_score, max_score, max_diff and v0 which can be understood as follows: The parameters min_score and max_score establish respectively the score values below and above which the classification of the pixel is set solely by the score. If score<min_score the pixel is classified as "unburned"; if score>max_score the pixel is classified as "burned". The parameters v0 (a number between 0 and 1) and max_diff (in days) establish the role of the detection dates in the image segmentation problem. If pixel X is a spatial neighbour of pixel Y, and if the detection dates for X and Y differ D days, then the value v(X,Y) of the connection between X and Y is a number between 0 and 1. V0 equals 1 when D=0 and decreases linearly to 0 until D = max_diff. Formally, v(X,Y) is defined as: if D > max_diff then v(X,Y) is 0; if D <= max_diff the value is v0 *(1-D/max_diff). Hence, the value of the connection between two neighbours is highest when the detection date for both neighbours is the same and vanishes to 0 when the dates of detection are more than max_diff days apart.

4.2.1.4.2 Graph

The vertices of the graph are the pixels with known score and detection dates. There are two additional vertices that represent the classes "burned" and "unburned". There are two types of edges in the graph. The first type of edges connect either the vertex "unburned" to a pixel X, or connect X to the vertex "burned". If for a pixel X, score<mean_score, where mean_score is the average of min_score and max_score, then there is a directed edge from the vertex "unburned" to the pixel X, with weight given by the logit of p_score. The variable p_score takes values in [0,0.5] and is defined by p_score = (score-min_score)/(max_score-min_score) if score > min_score, and it is the minimum value of those p_score if score<= min_score (to prevent p_score = 0). The logit function is defined by integer nearest to Logit $(p) = 100 * p/(1-p)$. If score >= mean_score for pixel X, there is a directed edge in the graph from X to "burned", with weight given by Logit(p_score), where p_score is defined as before, but takes values in [0.5,1], and is always lower than 1. The second type of edges in the graph connect pixels X and Y that have a positive value v(X,Y) as defined earlier. If X and Y are connected, then we add to the graph two directed edges, one from X to Y with weight Logit (v(X,Y)) and the other from Y to X with the same weight. As for the p_score, to prevent v = 0 or v = 1, we assign to it the minimum or maximum p_score value in the range (0,1). Figure 19 displays the topology of a MAP - MRF graph for an illustrative 10 * 10 pixel area.

4.2.1.4.3 Solution of the problem

The solution of the problem is the minimum source/sink-cut in the graph, where the source is the vertex "unburned" and the sink is the vertex "burned". The minimum cut defines a 2-partition of the pixels in the graph: the first element of the partition are the pixels connected to the vertex "unburned" and the second element of the partition are the pixels connected to the vertex "unburned". This partition gives the segmentation of the image into unburned and burned pixels.
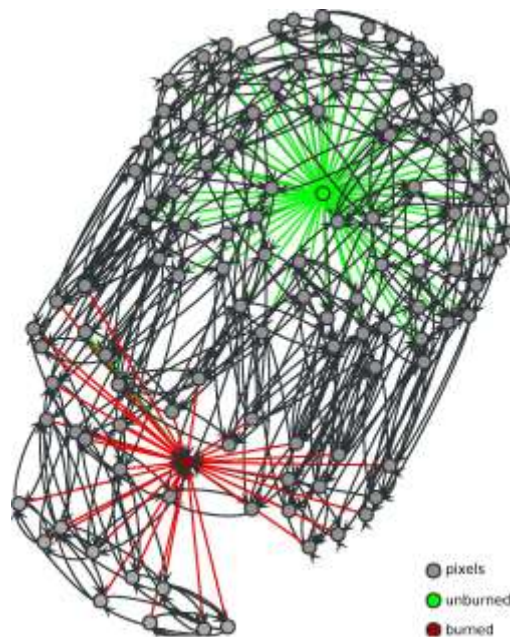
Figure 19: Topology of the graph of the MAP-MRF problem for a 10 x 10 pixel area. The pairs of connected pixels are spatial first-order neighbours and have detection dates at most 20 days apart. The solution of the MAP-MRF problem is partition of the pixels in an "unburned" and a "burned" component defined by the minimum cut in this graph.

Figure 20 displays the result of applying the Markov Random Field algorithm to the distance to ideal data (p-score) of Figure 198, using 0.5 as the threshold for initial assignment of pixels to the categories unburned (< 0.5) and burned (> 0.5).
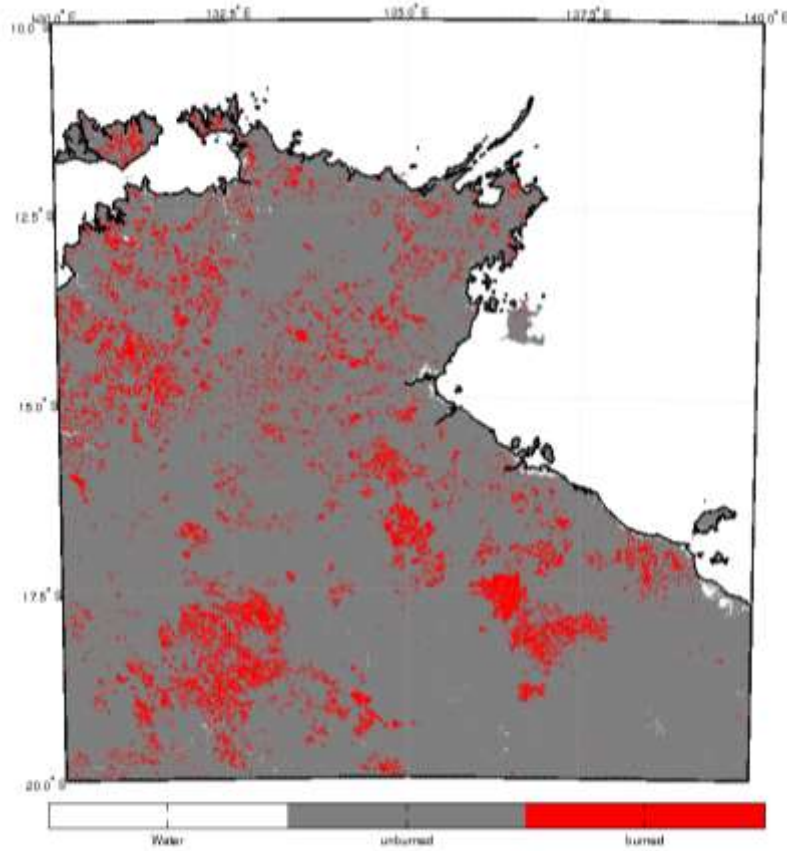
Figure 20: MRF revised burned area map, Australia, 2007

4.3   MERIS detailed algorithm description

When designing an algorithm on a global scale, it is necessary to take into account that the developed methodology is meant to be automatic and operational. Hence, the algorithm must be robust to account for potential problems in the input data, and as less site-dependent as possible, to tackle the very diverse regional burning conditions found worldwide. The most appropriate solution that satisfies these criteria is a hybrid approach using both thermal and reflectance data. The former detects active fires, and the latter the post-fire burned signal. In order to consider a proper balance between omission and commission errors, the algorithm includes two different phases: seed identification, which aims to minimize commission errors, and contextual analysis (region growing), which is mostly included to reduce omission errors.

The following sections describe in more detail the general structure of the algorithm and the two phases developed.

4.3.1 MERIS algorithm general scheme

Hybrid algorithms use post-fire spectral reflectances or reflectance changes together with thermal anomalies (active fires) to determine the Burned Area (BA) extent. Since both signals are complementary, the combination of spectral reflectance information with active fires to identify BA should provide a more reliable discrimination of BA areas. Several authors have shown these benefits in previous papers (Fraser et al. 2000; Giglio et al. 2009; Giglio et al. 2005; Roy et al. 1999), particularly with MERIS images (González-Alonso and Merino de Miguel 2009; González-Alonso et al. 2010).

Usually hybrid algorithms make use of hot spot information following two approaches:

 i) to estimate representative statistics of burned areas, by selecting reflectance values of a sample of burned pixels (a pixel is considered burned if it is associated to a hot spot), and then perform a burned/not burned classification of the remaining pixels (using Bayesian classifiers or other methods);

ii) to confirm that a pixel previously classified as burned is in fact burned, wherever the burned patch has a hot spot inside or in the vicinity.

In this case, we rely on the accuracy of MODIS Hotspot / Active Fire Detection Data set, (NASA FIRMS, 2012. MODIS Hotspot /Active Fire Detections. Data set. [http://earthdata.nasa.gov/firms].) to describe sampling points within fire perimeters, since they cover the period of MERIS operations. It is well known that HS do not provide a full description of fire-affected areas, as satellite sensors only detect those fires that are active when the satellite overpasses the fires. However, the high thermal contrast between burning and background pixels and the sensitivity of MODIS thermal channels, ensures a high confidence in detecting actual fires avoiding commission errors.

An exploratory analysis of HS performance was made to detect burned perimeters by comparing HS with our fire reference data extracted from Landsat TM/ETM+. Results have recently been published (Hantson et al., 2013). Commission errors found were very low (<3 %) for all study sites, but omission errors (burned patches undetected), were relatively high (>25%) particularly for small BA patches. While HS for labelling fire dates has been proposed by other authors (Boschetti et al. 2010) we rely on HS to establish the most appropriate data for the post-fire temporal compositing, given the limitations of MERIS data for detecting a strong BA signal

The MERIS BA algorithm specified here is based on the use of MERIS reflectance bands, spectral indices and both post-fire and multi-temporal analysis controlled by HS locations. Input data to the algorithm: spatial distribution of active fires (X,Y coordinates), MERIS reflectance bands 8 and 10, masks that were derived in the pre-processing chain of MERIS images (water, cloud, shadow, haze and snow masks), which are described in the ATBD v2.2 (Bachmann et al. 2014).

A general scheme of the MERIS BA algorithm is shown in Figure 21.
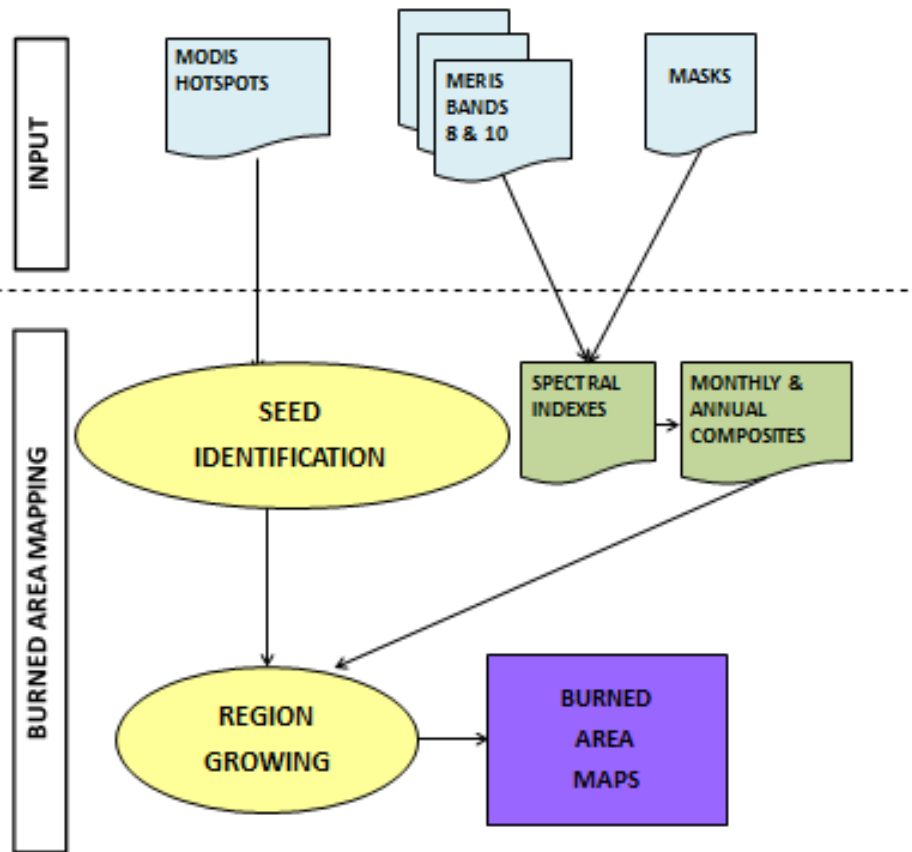
Figure 21: Approach for burned area detection algorithm

4.3.2 Generation of spectral indices

Spectral reflectance and mask information is used to obtain monthly and annual spectral reflectance and index composites (Figure 21). Following previous literature review and sensitivity analysis conducted within the fire_cci project, the near infrared reflectance (NIR) has been used together with the GEMI index (Pinty and Verstraete 1992) to discriminate BA. NIR and GEMI index have been extensively used for burned area mapping in different ecosystems (Barbosa et al, 1999b in Africa; Pereira, 1999 in a comparative study with AVHRR data; Chuvieco et al, 2002 in Mediterranean areas; Martin et al., 2005 in the Mediterranean; Chuvieco et al., 2008 in Boreal forest). GEMI expression is (Pinty and Verstraete 1992):

$$GEMI = \eta * (1 - 0,25\eta) - \frac{\rho_R - 0,125}{1 - \rho_R}$$

(8)

Where

$$\eta = \frac{2 * (\rho_{IR}^2 - \rho_R^2) + (1,5 * \rho_{IR}) + (0,5 * \rho_R)}{\rho_{IR} + \rho_R + 0,5}$$

(9)

GEMI and NIR should show a significant decrease when a fire occurs. This is commonly the case, as it is shown in Figure 22, but changes in the expected behaviour may be caused by other factors, such as clouds, shadows, haze, snow melting or flood.
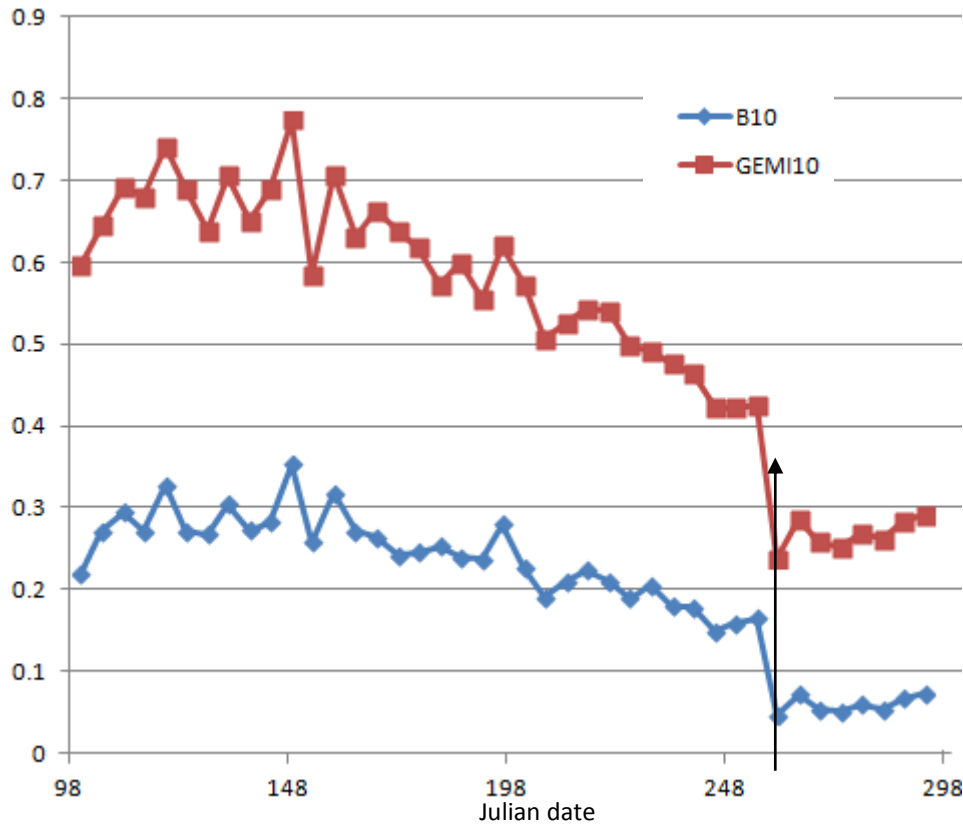
Figure 22: Temporal evolution GEMI and NIR reflectance (MERIS B10) for a burned pixel in Kazakhstan. The fire occurred at day 260, indicated by the arrow.

BA detection is performed in a two phase process: the first one aims to detect seed pixels (section 4.3.6) while the second one will develop contextual criteria around these seed pixels (section 4.3.7).

4.3.3 Mask threshold identification

All threshold values have been set empirically by performing several studies on a selection of images in all study sites. Final threshold selection is as follows:

- Cloud, snow, shadow and water masks: 30 %

- Haze: 40 %.

An example of the influence of the haze threshold is shown in Figure 23 and Figure 24. The values of bands 8 and 10 correspond to a pixel in Kazakhstan study site in 2005. In Figure 23 only the static water and cloud (< 30 % cloud coverage) masks have been applied. Shadow, haze and snow were not filtered. In Figure 24, static water, cloud (< 30 % coverage) and haze (< 40 % coverage) masks have been applied.
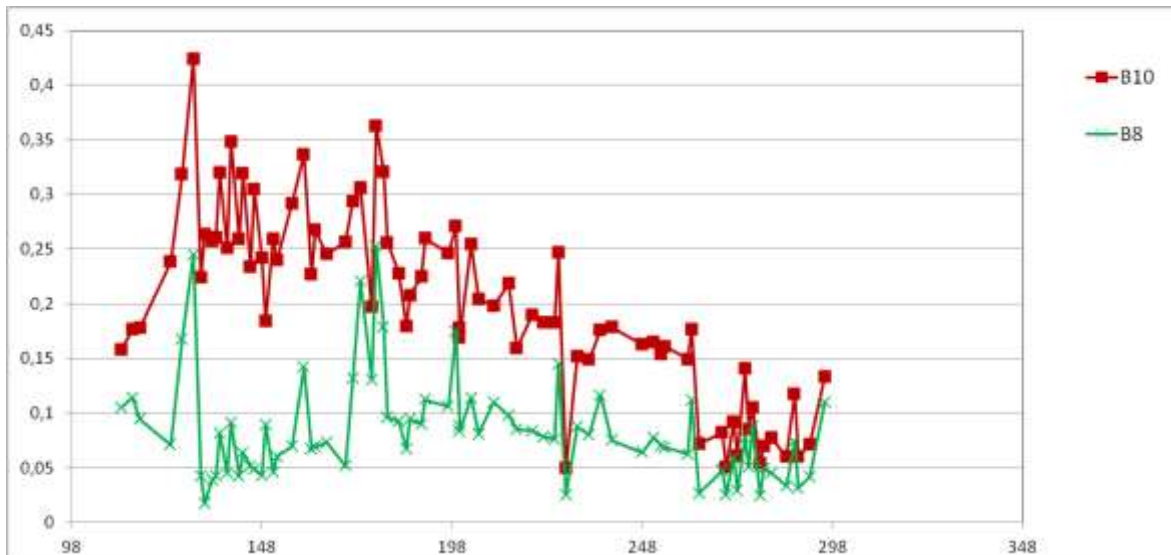
Figure 23: Temporal evolution of R and NIR reflectance for a pixel in Kazakhstan. All available images of the year with less than 30 % of clouds are included.
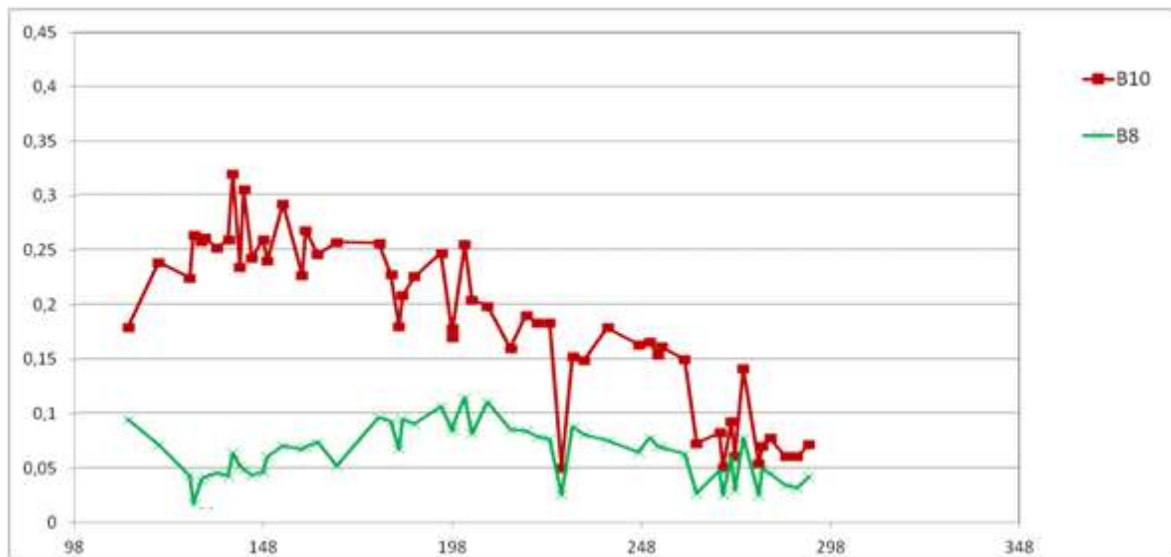
Figure 24: Temporal evolution of R and NIR reflectance for the same pixel represented in Figure 22. Images with haze > 40 % have been discarded.

As can be seen by comparing Figure 23 and Figure 24, equilibrium must be reached between image availability and noise reduction. A cloud threshold was established at 30 % after several tests with samples of images for different study sites. A more restrictive threshold would lead to lack of information for long time periods, especially in areas where clouds are a known permanent issue (Tropics). This value offers a good compromise between quality of the data filtered and number of observations discarded.

A numerical example of the procedure to set the haze threshold is shown hereafter and is illustrated in Table 2, Table 3 and Table 4. Figure 25 highlights the area in the Australian study site from where data have been extracted. Table 2 show the HS values for a small window (red box in Figure 25) of the Australian study site (pixels from (470:480, 1,240:1,250) for September 2005. The HS values are extracted from a Thiessen matrix, which is computed by obtaining for each pixel the closest HS and labelling it with the date of that HS. A more comprehensive explanation on the creation of the Thiessen matrix is given in section 4.3.3.3. Table 4 shows the dates of the first valid MERIS observation after the

date registered in the HS Thiessen matrix, when cloud and haze thresholds are set to 30. Table 4 shows the dates of the first valid MERIS observation after the date registered in the HS Thiessen matrix when cloud and haze thresholds are set to 30 and 40, respectively.

Figure 25: Australian study site, the red box corresponds to the area where values were extracted for Tables 2, 3 and 4 for September 2005.

Table 2: HS matrix dates.

271	271	271	271	271	271	267	267	267	267	267
271	271	271	271	271	271	267	267	267	267	267
271	271	271	271	271	267	267	267	267	267	267
271	271	271	271	267	267	267	267	267	267	267
271	271	271	267	267	267	267	267	267	267	267
271	267	267	267	267	267	267	267	267	267	267
267	267	267	267	267	267	267	267	267	267	267
267	267	267	267	267	267	267	267	267	267	267
267	267	267	267	267	267	267	267	267	267	267
267	267	267	267	267	267	267	267	267	267	267
268	267	267	267	267	267	267	267	267	267	267

Table 3: Dates for the composite when cloud and haze thresholds are set to 30.

272	300	300	300	300	300	300	300	-4	300	272
300	300	300	300	300	272	300	300	-4	300	300
300	300	300	-4	-4	300	300	300	300	300	300
300	300	300	-4	-4	-4	-4	300	300	300	300
300	272	300	-4	-4	-4	-4	-4	300	300	300
272	272	300	-4	-4	-4	-4	-4	300	300	300
300	300	300	300	-4	-4	-4	-4	300	300	300
300	300	300	300	-4	-4	-4	-4	300	300	300
300	300	300	300	300	-4	300	300	300	300	300
300	300	300	300	300	300	300	300	300	300	300
272	300	300	300	300	300	300	300	300	300	300

Table 4: Dates for the composite when cloud and haze thresholds are set to 30 and 40 respectively.

272	272	272	272	272	272	272	300	300	269	269
272	272	272	272	272	272	272	300	300	269	269
272	272	272	272	272	269	272	269	269	269	269
272	272	272	272	269	269	269	269	269	269	269
272	272	272	272	-4	269	269	269	269	269	269
272	272	272	300	-4	269	269	269	269	269	269
272	272	272	300	300	269	269	269	269	269	269
300	300	300	300	300	269	269	269	269	269	269
300	300	269	272	300	269	269	269	269	269	269
272	272	272	272	272	269	269	269	269	269	269
269	272	272	269	272	300	300	269	269	269	269

As can be concluded from the direct comparison of HS matrix Table 2 and the composite dates (Table 3), the dates obtained through the images available (Table 3) have a delay of about 30 days when compared to the HS dates, and for some pixels there is no valid data available within a 45 days range (-4 value). The conclusion is that a modification on the cloud threshold will not introduce relevant changes, but an increase in the haze threshold would. In Table 4, when the haze threshold is set to 40, most of the pixels have a date closer to the HS matrix obtained from the Thiessen polygons (Table 2) and most of the non-available data have been replaced by proper dates. Haze threshold is therefore set to 40.

4.3.4 Generation of post-fire composites and annual trends

MERIS temporal resolution characteristics and the exploratory analysis led to the conclusion that the best algorithm implementation would be based on a series of temporal composites. Two aspects have to be considered: the length of the compositing period and the criteria to select the most adequate pixel from the time series.

4.3.4.1   Compositing length

After analyzing different alternatives (from monthly to annual composites) the monthly composite option is selected. This length is a good balance between the number of images to obtain a cloud free composite while keeping the spectral contrast of the post-fire burned signal. The composite is generated with images from 60 consecutive days, but monthly aggregated. Therefore, 12 composites are obtained, each one of them containing information from the specific month and from the month after. Seed pixel identification and region growing phases of the algorithm are performed using the post-fire and annual reference composites. Generation of these composites is detailed in the following sections.

4.3.4.2   Post-fire composites: NIR-HS, GEMI-HS.

The compositing criterion should focus on emphasizing the post-fire reflectance signal. In order to do so, there is a need to establish a method to select the day with the most adequate observation, and the band or spectral index that will be computed for the selected date to obtain the final composite.

After exploring different possibilities developed for other sensors (Chuvieco et al. 2005) and different compositing techniques to obtain the monthly composite, the two implementations that present better results in terms of spatial or temporal consistency are:

4.3.4.3   Closest day to the HS

The idea behind this option is to select the date that will most likely be burned, following the HS spatial distribution. The computation of this composite is based on the Thiessen polygon matrix, which defines the area that is closer to a particular HS than to another HS. An example of this matrix is shown in Figure 26 for the Australian study site in October 2005. Spectral index values (GEMI) and NIR reflectance for the date obtained from the HS matrix are computed per pixel. If no data exists for that day or the data is considered not valid (it is filtered by the mask thresholds) the next available day is used to compute the spectral index and so on until the last day of the bi-monthly space is reached. The main advantage of this technique is that it ensures temporal consistency within the MERIS data. Nevertheless, when there are few fires, the Thiessen matrix creates artificial spatial structures that are not associated to fire events. This effect is also enhanced by the fact that images do not have any BRDF correction applied and hence images from different illumination and observation conditions are being used as equivalent. This issue may need resolving in later work to test the actual effect. An example of the Julian dates from the MERIS images that are being used to create the composite is shown in Figure 27. Figure 28 represents the NIR values associated to these dates; the spatial structures are highlighted with the red circle.
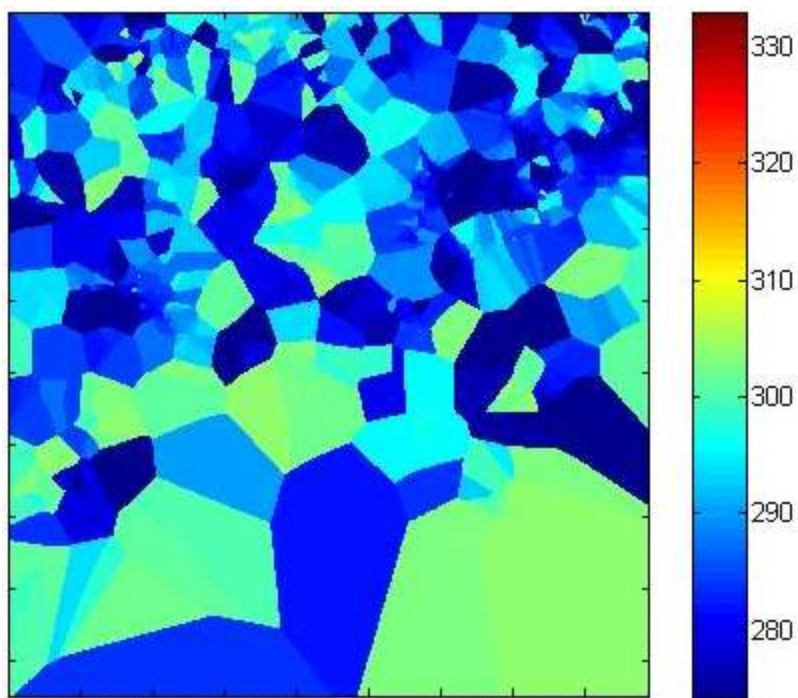
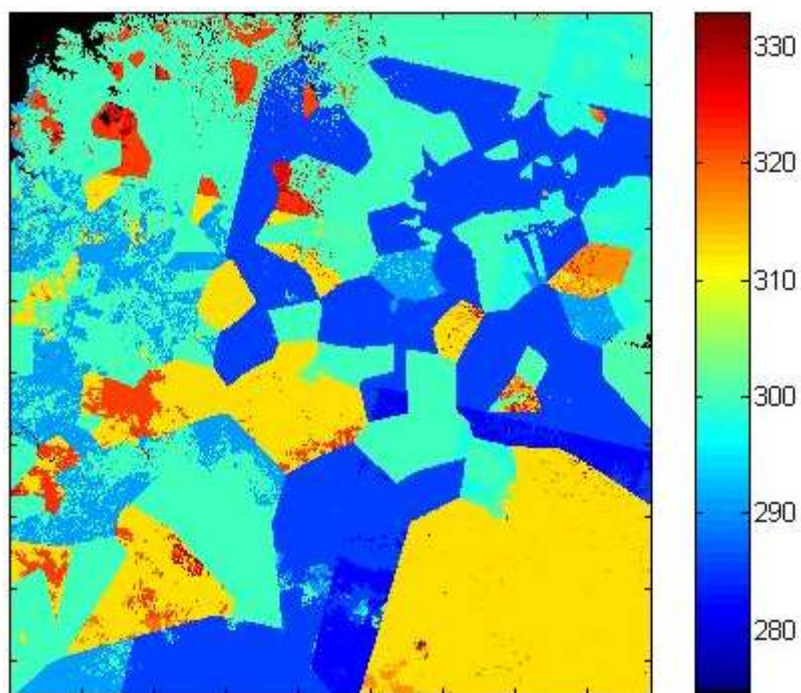**Figure 26: Thiessen matrix for Australian study site in October 2005**

Figure 27: Julian dates associated to MERIS images for Australia October 2005
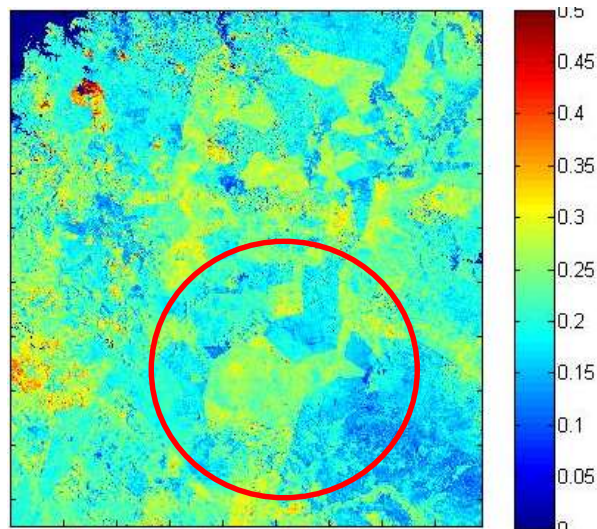
Figure 28: NIR reflectances related to the Julian dates in Figure 274

4.3.4.4   2nd NIR minima

The second technique is based on obtaining the 2nd lowest NIR value in a two month time series. The minimum NIR can be related to burned areas and avoids selection of clouds, but can be confused with cloud shadows, which also have a very low NIR reflectance. The second minimum should minimize this potential error. The use of lower values aims also at reducing the BRDF effect impact on the composite since values in the same range should be related to similar illumination and viewing conditions. This technique ensures a higher spatial consistency than the method in 4.3.3.3, as can be seen in Figure 29. The main drawback of this technique is that due to the variations in reflectance values over time, other changes not related to a fire (for instance cloud shadows) may be included in the composites, and therefore it can introduce commission or day detection errors. An example of the dates associated to the second minima NIR in October 2005 for the Australian study site is shown in Figure 30.
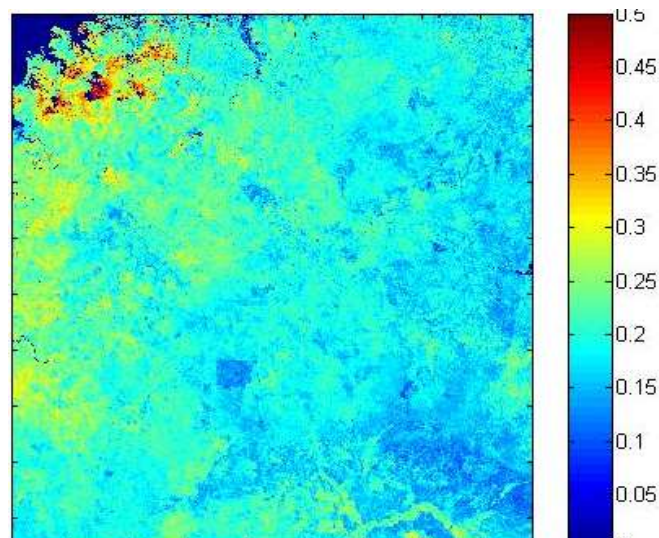

Figure 29: NIR second minima for October 2005 in the Australian study site
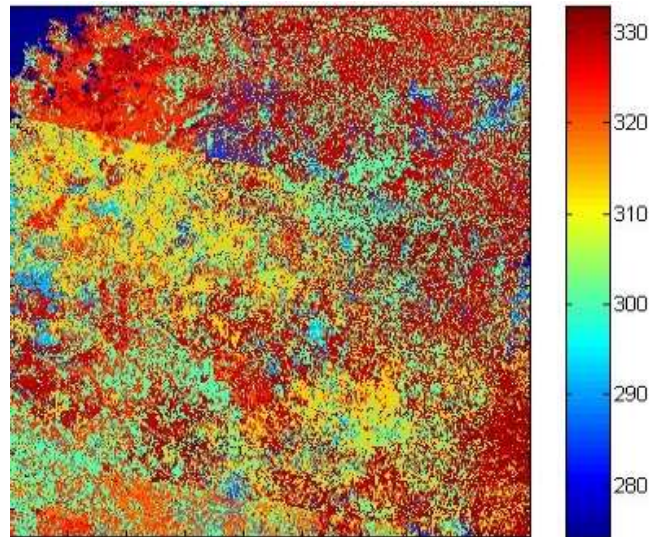
Figure 30: Julian dates associated to the selection of the NIR second minima

4.3.4.5 Final compositing criterion

The main driver for the methodology to create the monthly composite is to obtain a composite where the information is as spatially and temporally consistent as possible. Each one of the presented methodologies (introduced in 4.3.4.3 and 4.3.4.4.) covers one of these aspects. Therefore, it was decided to merge the two compositing techniques. The techniques were combined following the next steps:

- Build Thiessen matrix of the closest day to the HS
- Identify 3 NIR minima every 2 months

  - Closest minimum after the Thiessen matrix date is chosen.
  - If all minima occur before the HS date, the 2nd minimum is chosen.

If all minima occur before the HS date it is assumed that no fire occurred, therefore the 2nd minimum before the HS is chosen, in order to avoid possible cloud shadow effects.

The final composite includes therefore NIR reflectance from band 10. GEMI composite is also computed for the same dates identified using bands 8 and 10.

The result of combining both techniques leads to higher spatial and temporal consistency as shown in Figure 31 and Figure 32.
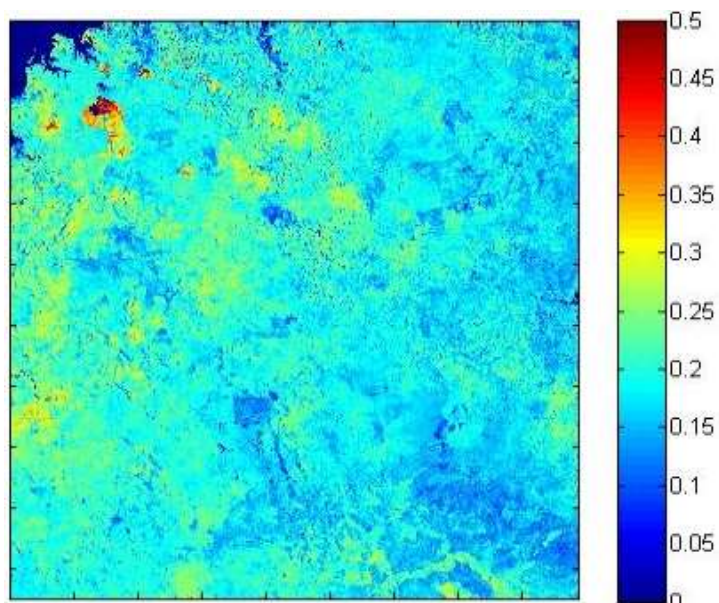
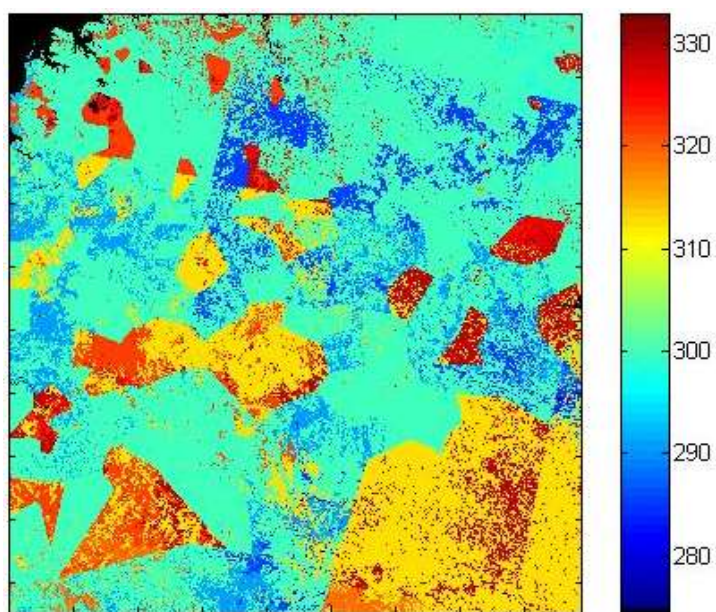**Figure 31: NIR final composite for Australia in October 2005**

Figure 32: Julian dates for Australia in October 2005

4.3.5 Annual reference trends

In addition to the post-fire composites, an annual reference composite is created. This annual composite is called DifGEMI and is obtained as the difference between the annual maximum GEMI value per year and the monthly GEMI-HS post-fire composite.

The annual maximum GEMI maximizes the GEMI value to account for the maximum seasonal greenness of each pixel. Pixel values for the annual series are selected in the period when vegetation has a maximum productivity. The monthly GEMI-HS composite accounts for the potential post-fire value. It was assumed that the change between annual maximum (Annual maximum GEMI) and the post-fire value (included in the GEMI monthly composite) should be the higher for burned pixels than for unburned ones, thus emphasizing post-fire spectral changes. Therefore, by obtaining the DifGEMI, the expected change between that maximum value and the post-fire value is the highest, helping to identify the areas that have burned.

Examples of these two composites and their difference for October 2005 are shown in Figure 33.
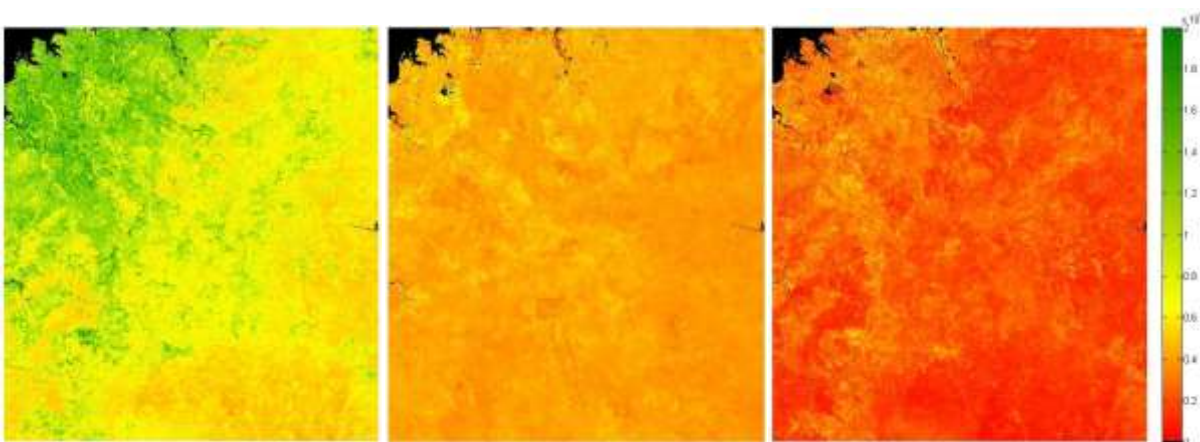
Figure 33: Maximum GEMI for 2005, GEMI in October 2005 and DifferenceGEMI composites for the Australian study site.

4.3.6 Seed selection

4.3.6.1 Criteria for selecting seed pixels

This phase is highly relevant in the BA detection algorithm. The objective is to select the most clearly burned pixels, from which a region growing algorithm is applied to obtain the final detection of the BA patch. The main goal of this phase is to avoid commission errors, as false seed pixels would create false BA patches on the growing phase. The seeds are selected on a monthly basis. This phase starts from the monthly composites, explained in the previous section.

Since spatial resolution of the MODIS HS is 1000 m, and the MERIS one is 300 m, the MERIS pixel within the vicinity of a HS that was more likely to have been burned should be selected. Therefore, the lowest value on the 3 x 3 MERIS pixels surrounding the MODIS HS coordinates (see Figure 34) is identified.

Figure 34: HS vs MERIS pixels.

To avoid commission errors, we introduce an additional temporal change constrain to the MERIS pixels identified, and accept only pixels that showed a NIR reflectance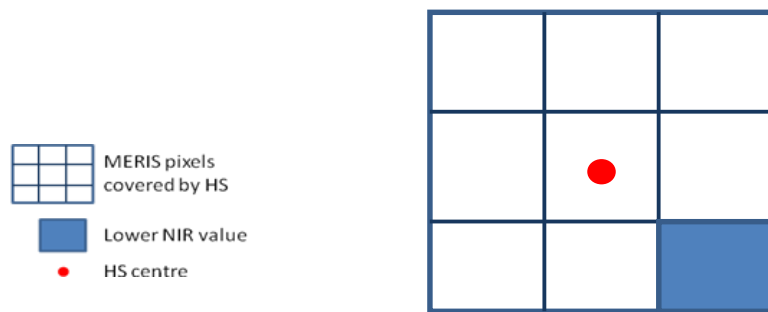 decrease in time t from the previous period t-1, as burned areas should always have a lower signal than before the fire.
These pixels are named potential active fires (PAFs).

4.3.6.2   Identification of burned statistics

Once the PAFs are selected, two cumulative distribution functions of burned and unburned (CDFs) are built. Burned pixels are at this stage identified by the PAFs from the previous phase (4.3.6.1), while unburned pixels are selected as those that do not have a HS in a matrix of 64 x 64 pixels and that have not been classified as burned in the previous months. These frequency curves are built for each monthly composite and study site. In terms of global processing the corrected reflectances are gridded into tiles of 10 x 10 degrees (3,600 x 3,600 pixels at MERIS spatial resolution). These tiles are the input files for all processes of the MERIS BA algorithm. Therefore the same procedure described here is applied to the 10 x 10 degrees tiles to identify burned statistics.

Cumulative frequency curves are derived from both distributions (Figure 35). These curves are used to define a NIR burned threshold (TB). The closer the curves the more pixel values are shared by the burned and unburned distributions. This implies less capacity to discriminate between burned and unburned pixels.

The threshold value of the burned signal is defined as the first decile of the burned curve below the decile 1 of the unburned curve. If the curves are well separated then the burned decile should be higher (and more values will pass the threshold condition) than if the curves are close to each other. An example of a case with worse separation is shown in Figure 35a, and represents the values obtained for May 2008 in Canada (tile L03C07). An example of a case with better separation between classes is shown in Figure 35b. It corresponds to June 2008 in South Africa (tile L11C20).
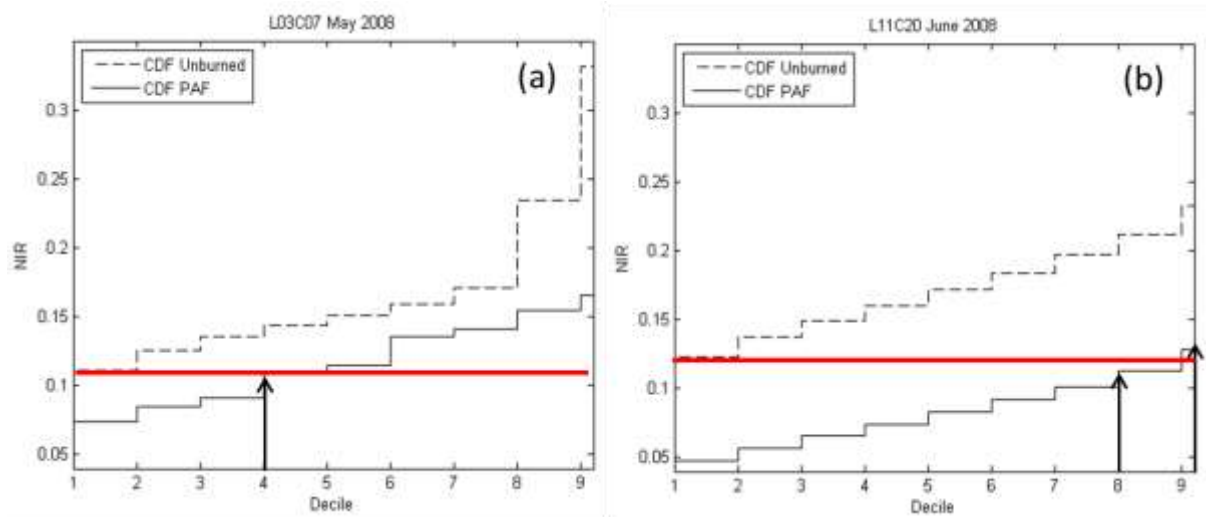
Figure 35: Threshold based on decile 10 of the unburned CDF for cases with worse (a) and better (b) separation between classes, correspondent to May 2008 in tile L03C07 (Canada) and June 2008 in L11C20 (South Africa) respectively. In a) TB for seed and growing phases remains the same (single arrow). In b) TB for the seed phase corresponds to decile 8 (left arrow) and TB for the growing phase corresponds to decile 9 (right arrow).

4.3.6.3   Final seed selection

The final step to classify a pixel as seed verifies three conditions:

- The NIR value has to be lower than the TB threshold identified.

- There is a PAF identified (from applying step 1 and 2 detailed in sections 4.3.6.2.) in a 9 x 9 matrix around the pixel being classified.

- The difference in NIR values from the composite in month N and the previous month is a negative value, to ensure that for the pixels in the 9 x 9 matrix there is a drop in NIR reflectance.

A scheme illustrating this procedure is shown in Figure 36:

Figure 36: Diagram for seed selection

4.3.7 Region growing

This phase focuses on improving the delimitation of BA patches applying contextual algorithms to the seed pixels. Those pixels located in the neighbourhood of the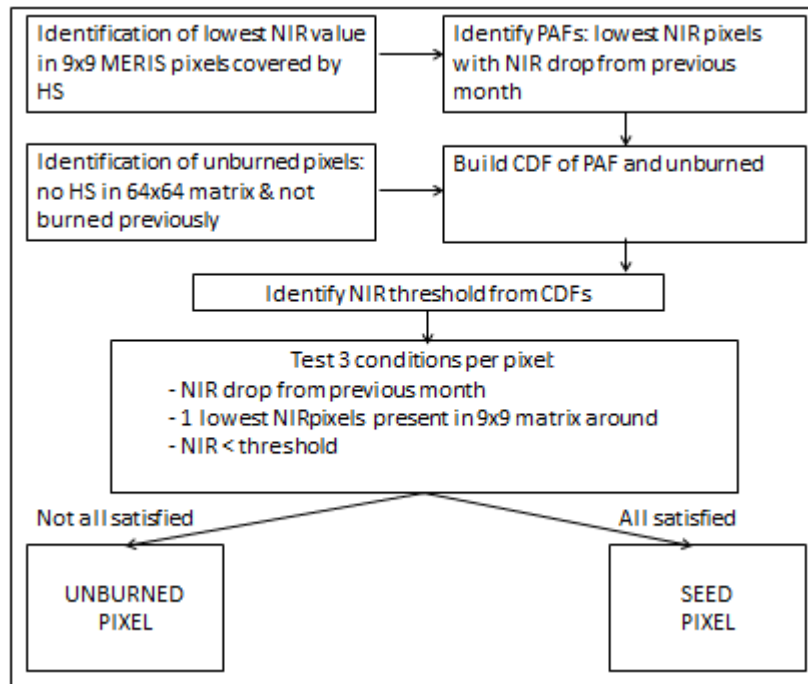 seed pixels are candidates to extend the BA area if they fulfill additional requirements in terms of spectral similarity with the seed pixels and of new thresholds defined for this phase.

In this case 3 conditions need to be verified by the pixels surrounding a seed to be classified as burned:

- NIR threshold value is reviewed in this phase. The threshold is modified according to the ability to distinguish between burned and unburned classes identified in the seed phase. Assuming a normal distribution, if the burned decile used to define the seed threshold is 7 or higher, the burned/unburned curves cross after at least one standard deviation of the mean burned values. In those cases the ability to distinguish between burned and unburned classes is considered high. Therefore, the new threshold condition for the growing phase is raised up to the decile 9 of the burned pixels curve (Figure 35b). If the burned decile used to define the seed threshold is lower than 7 then the ability to discriminate burned and unburned classes is considered low. In this case, in order to ensure less commission errors in the growing phase, the threshold will be the one defined in the seed phase.

- The diffGEMI annual composite has to verify a decreasing threshold between seed and neighbour pixels. Pixels will be classified as burned if the neighbours to a seed pixel have higher values than the threshold. The threshold is defined from the diffGEMI value found in the seed pixel multiplied by 0.9.

- The third condition relies on a minimum drop that has to be verified for each pixel. The decrease in the NIR values (DNIR) between t and t-1 for each candidate BA pixel has to be higher than the decrease observed for unburned areas. With this criterion the aim is to avoid neighbor areas to the seeds that might have fire-unrelated changes.

A final test is applied to avoid large commission errors in a few areas with dark covers, where the region growing process might not perform properly (specific regions of Australia, China and India, for instance). In this case, we filter out large polygons when the number of burned pixels exceeded largely the number of hotspots. We established an empirical value of 30 times (MERIS BA pixels/HS), based on previous findings from Hantson et al. (2013), who compared the distribution of HS and Landsat-derived burned patches in the same study sites used to develop this algorithm.

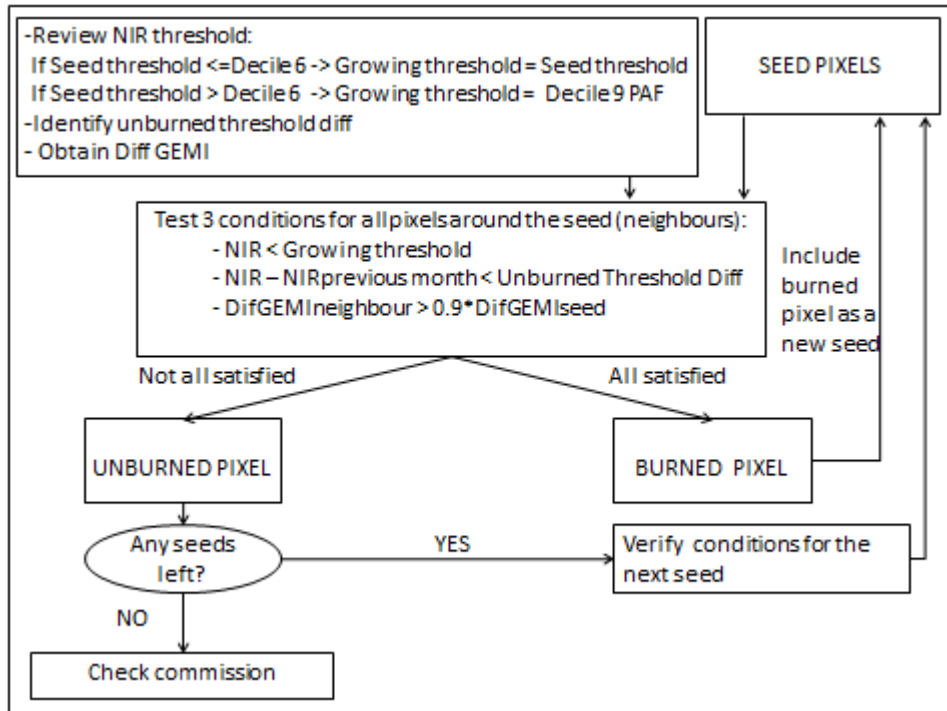Figure 37 shows a scheme of the region growing phase.

Figure 37: Region growing phase

A final product example is shown in Figure 38. Julian dates of BA obtained for year 2006 in the Australian study site are represented.
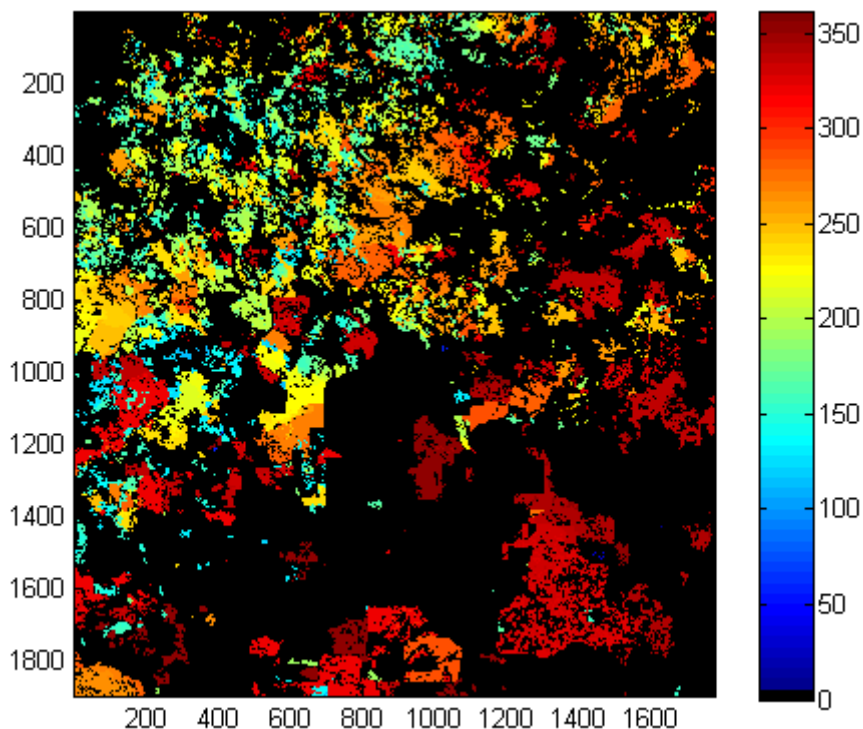

Figure 38: Julian dates of burned areas identified with the MERIS BA algorithm for the Australian study site in year 2006.

5 References

Auger, I. E. and Lawrence, C. E. (1989). Algorithms for the optimal identification of segment neighborhoods. *Bulletin of Mathematical Biology*, 51(1): 39-54.

Bachmann, M., E. Borg, B. Fichtelmann, K. Günther, T. Krauß, A. Müller, R. Müller, R. Richter, M. Wurm (2014) Algorithm Theoretical Basis Document – Volume I – Pre-processing. Fire_cci_Ph2_DLR_D3_6_1_ATBD_I_v2_2, https://www.esa-fire-ci.org

Barbosa, P.M., Grègoire, J.-M., Pereira, J.M.C. (1999b): An algorithm for extracting burned areas from time series of AVHRR GAC data applied at a continental scale. *Remote Sensing of Environment*, 69(3): 253-263.

Barbosa, P.M., Stroppiana, D., Grègorie, J.M., Pereira, J.M.C. (1999a): An assessment of vegetation fire in Africa (1981–1991): Burned areas, burned biomass, and atmospheric emissions, *Global Biogeochemical Cycles*, 13(4), 933–950.

Besag, J. (1986) On the statistical analysis of dirty pictures. *Journal of the Royal Statistical Society. Series B*, 48(3):259-302.

Bittencourt, H.R., Clarke, R.T. (2003b): Use of Classification and Regression Trees (CART) to Classify Remotely-Sensed Digital Images. Proc. 2003 IEEE International Geoscience and Remote Sensing Symposium, Toulouse, France, July 21-25, pp. 3751-3753.

Boardman, J.W., Kruse, F.A. and Green, R.O. (1995): Mapping target signatures via partial unmixing of AVIRIS data. Summaries of the 5th Jet Propulsion Laboratory (JPL) Airbone Earth Science Workshop, Pasadena, California, California Institute of Technology, 23-26.

Boschetti, L., Roy, D.P., Justice, C.O., & Giglio, L. (2010). Global assessment of the temporal reporting accuracy and precision of the MODIS burned area product. *International Journal of Wildland Fire, 19*, 705-709.

Boykov, Y., O. Veksler, and R. Zabih (2001). Fast approximation energy minimization via graph cuts. *IEEE Transactions in Pattern Recognition and Machine Intelligence*, 23(11):1222-1239.

Breiman, L., Friedman, J.H., Olshen, R.A. and STONE, C.J. (1984): Classification and regression trees. Beltmon, CA, Wadsworth Int.

Calado, T. Chuvieco, E., Günther, K.P., Oliva, P. Sandow, C. (2011): Data Access Requirements Document, Fire_cci_Ph1_UAH_D1_3_DARD_v1_7.pdf , https://www.esa-fire-ci.org/webfm_send/189

Carmona-Moreno, C., Belward, A., Malingreau, J.-P., Hartley, A., Garcia-Alegre, M., Antonovskiy, M.L., Buchshtaber, V. and Pivovarov, V. (2005): Characterizing interannual variations in global fire calendar using data from Earth observing satellites. Global Change Biology (2005) 11, 1537–1555, doi: 10.1111/j.1365-2486.2005.001003.x.

Carta, J. A., Buena, C., Ramírez, P. (2008). Statistical modelling of directional wind speeds using mixtures of von Mises distributions: Case study. *Energy Conversion and Management*, 49, 897-907.

Chang, D. and Song, Y. (2009): Comparison of L3JRC and MODIS global burned area products from 2000 to 2007, *J. Geophys. Res.*, 114, D16106, doi:10.1029/2008JD011361.

Chib, S. (1998). Estimation and comparison of multiple change-point models. *Journal of Econometrics*, 86: 221-241.

Chuvieco, E. (2008): Satellite observation of biomass burning: implications in global change research. Earth Observation and Global Change. E. Chuvieco. New York, Springer: 109-142.

Chuvieco, E. Opazo, S., Sione, W., Del Valle, H., Anaya, J., Di Bella, C., Cruz, I., Manzo, L., López, G., Mari, N., González-Alonso, F., Morelli, F., Setzer, A., Csiszar, I., Kanpandegi, J.A., Bastarrika, A. and Libonati, R. (2008a): Global burned land estimation in Latin america using MODIS composite data. Ecological Applications, 18, 64-79.

Chuvieco, E., Englefield P., Trishchenko, A.P. and Luo, Y. (2008b): Generation of long time series of burn area maps of the boreal forest from NOAA–AVHRR composite data. Remote Sensing of Environment vol. 112(5): 2381-2396.

Chuvieco, E., Giglio, L. and Justice, C. (2008c): Global characterization of fire activity: toward defining fire regimes from Earth observation data. Global Change Biology 14: 1488- 1502.

Chuvieco, E., De Santis, A., Riaño, D. and Halligan, K. (2007): Simulation approaches for burn severity estimation using remotely sensed images. *Journal of Fire Ecology, 3*, 129-150.

Chuvieco, E., Martín, M.P., & Palacios, A. (2002). Assessment of different spectral indices in the red-near-infrared spectral domain for burned land discrimination. *International Journal of Remote Sensing, 23*, 5103-5110.

Chuvieco, E. and Martín, M.P. (1994): Global fire mapping and fire danger estimation using AVHRR images. Photogrammetric Engineering and Remote Sensing, 60: 563-570.

Clark, R.N. and Roush, T.L. (1984): Reflectance spectroscopy: Quantitative analysis techniques for remote sensing applications. Journal of Geophysical Research 89: 6329-6340.

Coleman, T. F., & Li, Y. (1994). On the Convergence of Reflective Newton Methods for Large-Scale Nonlinear Minimization Subject to Bounds. *Mathematical Programming*, 67(2), 189-224.

Crawley, M.J. (2007) The R Book. Wiley-Blackwell, 950 p.

Dubovik, O., Holben, B., Eck, T. F., Smirnov, A., Kaufman, Y. J., King, M. D., Tanre, D. and Slutsker, I. (2002): Variability of absorption and optical properties of key aerosol types observed in worldwide locations, J. Atmos. Sci., 59, 590-608.

Ershov, D.V. and Novik, V.P. (2001): Mapping burned areas in Russia with SPOT4 VEGETATION (S1 product) imagery, final report, Contract 18176-2001-07-F1EI ISP RU, Eur. Comm. Joint Res. Cent., Brussels.

Eva, H. and Lambin, E.F. (1998): Burnt area mapping in Central Africa using ATSR data, Int. J. Remote Sens., 19, 3473– 3497.

Fisher, N.I. (1995). Statistical Analysis of Circular Data. Revised edition. Cambridge University Press.

Fraser, R.H., Li, Z. and Cihlar, J. (2000): Hotspot and NDVI differencing synergy (HANDS): a new technique for burned area mapping over boreal forest. Remote Sensing of Environment, 74, 362−376.

Fried, R. (2004) Robust filtering of time series with trends. *Nonparametric Statistics*, 16(3–4): 313–328.

Fried, R., K. Schettlinger and M. Borowski (2011). robfilter: Robust Time Series Filters. R package version 3.0. http://CRAN.R-project.org/package=robfilter.

Friedl, M.A. and Brodley, C.E. (1997): Decision tree classification of land cover from remotely sensed data. Remote Sensing of Environment 61: 399-409.

Gather, U., Fried, R. (2004), Methods and Algorithms for Robust Filtering, COMPSTAT 2004: *Proceedings in Computational Statistics*, J. Antoch (eds.), Physika-Verlag, Heidelberg, 159-170.

Geman, S. and S. Geman (1984) Stochastic relaxation, Gibbs distributions, and the Bayesian restoration of images. IEEE *Transactions in Pattern Recognition and Machine Intelligence*, 6(6): 721-741.

Giglio, L., I. Csiszar, and C.O. Justice (2006) Global distribution and seasonality of active fires as observed with the Terra and Aqua Moderate Resolution Imaging Spectroradiometer (MODIS) sensors. *Journal of Geophysical Research*, 111, G02016, doi:10.1029/2005JG000142.

Giglio, L., Loboda, T., Roy, D.P., Quayle, B. and Justice, C.O. (2009): An active-fire based burned area mapping algorithm for the MODIS sensor. Remote Sensing of Environment 113: 408-420.

Giglio, L., van der Werf, G.R., Randerson, J.T., Collatz, G.J. and Kasibhatla, P. (2006b): Global estimation of burned area using MODIS active fire observations. *Atmospheric Chemistry and Physics* 6: 957-974.

Global Climate Observing System (GCOS) (2009). Guidelines for the generation of satellite-based datasets and products meeting GCOS requirements. Geneva: World Meteorological Organization

GlobCarbon (2007). Demonstration Products and Qualification Report. In (pp. 1-69): ESA

González-Alonso, F. and Merino-de-Miguel, S. (2009): Integration of AWiFS and MODIS active fire data for burn mapping at regional level using the Burned Area Synergic Algorithm (BASA). International Journal of Wildland Fire, 18, 404-414.

González-Alonso,F., Merino de Miguel, S. and Huesca, M. (2010): A burned area synergistic algorithm using MERIS-ENVISAT images and MODIS thermal anomalies. ESA Living Planet Symposium. Bergen. June, 2010

González-Alonso, F., Salgado, V., Calle, V., Casanova, J.L., Sanz, J., de la Fuente, D., Goldammer, J.G., Li, Z., Qin, X., Zhang, X., Deng, G., Liu, Q., Li, G., Cai, H. and Huang, Z. (2009): Forest burn in China by means of MERIS and MODIS images. 2009 Dragon 2 Symposium, June 2009, Barcelona.

Govaerts, Y.M., Pereira, J.M., Pinty, B. and Mota, B. (2002): Impact of fires on surface albedo dynamics over the African continent, *107, 4629, doi:10.1029/2002JD002388.*

Greig, D.M., B.T. Porteous, and A.H. Seheult (1989). Exact maximum a posteriori estimation for binary images. *Journal of the Royal Statistical Society, Series B*, 51(2):271-279.

Hinkley, D. V. (1970). Inference about the change-point in a sequence of random variables. *Biometrika*, 57: 1-17.

Huang, S. and Siegert, F. (2004): ENVISAT multisensor data for fire monitoring and impact assessment. International Journal of Remote Sensing 25(20): 4411-4416.

IPCC Fourth Assessment Report: Climate Change (2007) (AR4).

Iqbal, M. (1983): An Introduction to solar radiation. Academic Press, New York.

Jacob, D.J. (1999): Introduction to atmospheric chemistry. (Princeton University Press: Princeton).

Jones, T.A. (2006). MATLAB functions to analyze directional (azimuthal) data − I: Single-sample inference. *Computers & Geosciences*, 32, 166-175.

Jong, K., Marchiori, E., Meijer, G., Vaart, A. v. d., and Ylstra, B. (2004). Breakpoint identification and smoothing of array comparative genomic hybridization data. *Bioinformatics*, 20(18): 3636-3637.

Kaufman, Y. J., Tanré, D., Remer, L.A., Vermote, E.F., Chu, D.A., and Holben, B.N. (1997): Remote sensing of tropospheric aerosol from EOS-MODIS over the land using dark targets and dynamic aerosol models, J. Geophys. Res., 102, 17,051– 17,067.

Kaufman, Y.J. and Justice, C.O. (1998): MODIS Fire Products Algorithm Technical Background Document (Version 2.2). Available at:
http://eospso.gsfc.nasa.gov/ftp_ATBD/REVIEW/MODIS/ATBD-MOD-14/atbd-mod-14.pdf

Kaufman, Y.J., Martins, J.V., Remer, L.A., Schoebrel, M.R. and Yamasoe, M.A., (2002): Satellite retrieval of aerosol absorption over the sunglint. Geophysical Research Letters, vol. 29, 19, 1928. doi: 10.1029/2002GL015403.

Killick, R. and Eckley, I. A. (2010). R package- changepoint: Analysis of Changepoint Models. Lancaster University, Lancaster, UK.

Killick, R., Fearnhead, P., and Eckley, I. A. (2012). Optimal detection of changepoints with a linear computational cost. *In Submission*.

Kugiumtzis, D. and A. Tsimpiris (2010). Measures of Analysis of Time Series (MATS): A MATLAB toolkit for computation of multiple measures on time series data bases. *Journal of Statistical Software*, 33(5): 1-30.

Kumar, R., & Silva, L.F. (1977). Separability of agricultural cover types by remote sensing in the visible and infrared wavelength regions. *IEEE Transactions on Geoscience Electronics, 15*, 49-59.

Le Page, Y., D. Oom, J.M.N. Silva, P. Jönsson, and J.M.C. Pereira (2010) Seasonality of vegetation fires as modified by human action: observing the deviation from eco-climatic fire regimes. *Global Ecology and Biogeography*. 19 (4): 575-588. DOI: 10.1111/j.1466-8238.2010.00525.x

Le Page, Y., J.M.C. Pereira, R. Trigo, C. da Camara, D. Oom, and B. Mota (2008) Global fire activity patterns (1996–2006) and climatic influence: an analysis using the World Fire Atlas. *Atmospheric Chemistry and Physics*, 8, 1911–1924.

Lobert, J.M. and Warnatz, J. (1993): Emissions from the combustion process in vegetation. In PJ Crutzen and JG Goldammer (Eds.) *Fire in the Environment: the Ecological, Atmospheric, and Climatic Importance of Vegetation Fires*. John Wiley and Sons,Chichester, UK.

Loh, W.Y. and Shih, Y.-S. (1997): Split selection methods for classification trees. Statistica Sinica 7: 815-840.

Mardia, K.V., Jupp, P.E. (2000). *Directional Statistics*. 2nd ed. New York: John Wiley and Sons.

Martín, M.P., Gomez, I. and Chuvieco, E. (2006): Burned Area Index (BAIM) for burned area discrimination at regional scale using MODIS data. Forest Ecology and Management, 234S, S221.

Martín, M.P. (1998). Cartografía e inventario de incendios forestales en la Península Ibérica a partir de imágenes NOAA-AVHRR. In, *Departamento de Geografía*. Alcalá de Henares: Universidad de Alcalá.

Mather, P.M., & Coch, M. (2011). Computer Processing of Remotely Sensed Images, 4th Edition. Chichester: John Wiley & Sons.

Moreno-Ruiz, J.A., Barbosa, P.M., Carmona-Moreno, C., Gregoire, J.M., Belward, A.S. (1999): GLINTS-BS – Global Burn Scar Detection System. European Union Technical Note I.99.167. May 1999.

Mota, B., J.M.C. Pereira, D. Oom, M.J.P. Vasconcelos, and M. Schultz (2006). Screening the ESA ATSR-2 World Fire Atlas (1997-2002). *Atmospheric Chemistry and Physics*, 6: 1409-1424.

Mutanga, O., Skidmore, A.K. and Prins, H.H.T. (2004): Predicting in situ pasture quality in the Kruger National Park, South Africa, using continuum-removed absorption features. Remote Sensing of Environment 89: 393-408.

Nash, J. E., & Sutcliffe, J. V. (1970). River flow forecasting through conceptual models part I — A discussion of principles. *Journal of Hydrology*, 10 (3), 282–290.

Oliva, P. (2009): Métodos para la cartografía de área quemada con imágenes del sensor envisat-meris en la cuenca mediterránea, Ph. D. Dissertation, University of Alcalá .

Oliva, P. and Martín, M.P. (2007): Mapping burned area by using Spectral Angle Mapper in MERIS images. In Proceedings of 6th International workshop on remote Sensing and GIS Applications to Forest Fire Management: Fire Effects Assessment. Thessaloniki, Greece, September 2007.

Oliva, P., Martín, M.P. and Chuvieco, E. (2010): Burned area mapping with MERIS post-fire image. International Journal of Remote Sensing in press.

Oom, D., J.M.C. Pereira (2013) Spatial autocorrelation in global vegetation fires: exploratory analysis of screened MODIS hotspot data. *International Journal of Earth Observation and Geoinformation*.

Padilla, M., Oliva P. and Chuvieco, E. (2012): Product Validation and Algorithm Selection Report, Fire_cci_Ph2_UAH_D2_5_PVASR_v2_0.pdf, http://www.esa-fire-cci.org/webfm_send/581

Peel M.C, Finlayson B.L, McMahon T.A, (2007) Updated world map of the Köppen-Geiger climate classification. Hydrol. Earth Syst. Sci. 11 (5): 1633-1644.

Pereira, J.M.C. (2003): Remote sensing of burned areas in tropical savannas. International Journal of Wildland Fire 12 (3-4):259-270.

Pereira, J.M.C., Flasse, S., Hoffman, A., Pereira, J.A.R., González-Alonso, F. and Trigg, S. (2000): Operational use of remote sensing for fire monitoring and management: regional case studies. In F. Ahern, J.-M. Grégoire and C. Justice, (Eds.), Forest Fire Monitoring and Mapping: A Component of Global Observation of Forest Cover (pp. 98-110). European Commission, Joint Research Centre, EUR 19588 EN.

Pereira, J.M.C. (1999): A comparative evaluation of NOAA/AVHRR vegetation indexes for burned surface detection and mapping. IEEE Transactions on Geoscience and Remote Sensing, 37(1), 217-226.

Pereira, J.M.C., Pereira, B.S., Barbosa, P., Stroppiana, D., Vasconcelos, M.J.P. and Grégoire, J-M. (1999a): Satellite monitoring of fire in the EXPRESSO study area during the 1996 dry season experiment: active fires, burnt area and atmospheric emissions. *Journal of Geophysical Research*, 104, D23: 30,701-30,712

Pereira, J.M.C., A.C.L. Sá, A.M.O. Sousa, J.M.N. Silva, T.N. Santos, e J.M.B. Carreiras (1999b) Spectral characterisation and discrimination of burnt areas. Em Remote Sensing of Large Wildfires in the European Mediterranean Basin, pp.123-138 (E. Chuvieco, ed), Springer-Verlag, Berlin.

Pereira, J.M.C, Sousa, A.M.O., Sá, A.C.L. (1999c): Regional-scale burnt area mapping in Southern Europe using NOAA-AVHHR 1 km data. In 'Remote sensing of large wildfires'. (Ed. EP Chuvieco) pp. 139–155. (Springer: Berlin).

Pereira, J.M.C. and Setzer, A.W. (1993): Spectral characteristics of fire scars in Landsat-5 TM images of Amazonia. International Journal of Remote Sensing, 14, 2061–2078.

Piccolini, I. (1998: Development and validation of an adaptive algorithm for burn scar detection using ERS/ATSR-2 data, Ph.D. thesis, Univ. La Sapienza, Rome.

Pinty, B., & Verstraete, M.M. (1992). GEMI: a non-linear index to monitor global vegetation from satellites. *Vegetatio, 101*, 15-20.

Plummer, S., Arino, O., Simon, M. and Steffen, W. (2006): Establishing an earth observation product service for the terrestrial carbon community: The GLOBCARBON Initiative. Mitigation and adaptation strategies for Global Change 11: 97-111.

Rast, M., Bézy, J.L. and Bruzzi, S. (1999): The ESA Medium Resolution Imaging Spectrometer MERIS - a review of the instrument and its mission. International Journal of Remote Sensing 20(9): 1681-1702

Riaño, D., Moreno Ruiz, J.A., Isidoro, D. and Ustin, S.L. (2007): Global spatial patterns and temporal trends of burned area between 1981 and 2000 using NOAA-NASA Pathfinder. Global Change Biology (2007) 13, 40–50.

Robinson, J.M. (1991: Problems in global fire evaluation: is remote sensing the solution? In 'Global Biomass Burning: Atmospheric, Climatic, and Biospheric Implications' (Ed JS Levine) pp. 67-73. (MIT Press: Cambridge, MA).

Roldán-Zamarrón, A., Merino de Miguel, S., González-Alonso, F., García-Gigorro, S. and Cuevas, J.M. (2006): Minas de Rio Tinto (south Spain) forest fire: Burned area assessment and fire severity mapping using Landsat 5-TM, Envisat-MERIS, and Terra-MODIS postfire images. Journal of Geophysical Research 111(G04S11).

Rousseeuw, J., Croux, C. (1993): Alternative to the median absolute deviation. Journal of the American Statisticak Association, Vol. 88, nº 424.

Roy, D. and Boschetti, L. (2009): Southern Africa Validation of the MODIS, L3JRC and GlobCarbon Burned Area Products. IEEE transactions on Geoscience and Remote Sensing, 47, 4, 1032 – 1044, doi:10.1109/TGRS.2008.2009000

Roy, D., Boschetti L., Justice, C.O. and Ju, J. (2008): The collection 5 MODIS burned area product - Global evaluation by comparison with the MODIS active fire product. Remote Sensing of Environment 112: 3690-3707.

Roy, D.P., Lewis, P.E. and Justice, C.O. (2002): Burned area mapping using multi-temporal moderate spatial resolution data—a bi-directional reflectance model-based expectation approach. *Remote Sensing of Environment*, 83, 263–286.

Roy, D.P., Giglio, L., Kendall, J.D., & Justice, C.O. (1999). Multi-temporal active-fire based burn scar detection algorithm. *International Journal of Remote Sensing, 20*, 1031-1038.

Schowengerdt, R.A. (2007). Remote sensing, models, and methods for image processing. Burlington, MA: Elsevier Academic Press.

Schwarz, G. (1978). Estimating the dimension of a model. *The Annals of Statistics*, 6(2): 461-464.

Scott, A. J. and Knott, M. (1974). A cluster analysis method for grouping means in the analysis of variance. *Biometrics*, 30(3): 507-512.

Silva, J.M.N., Pereira, J.M.C., Cabral, A., Sá, A.C.L., Vasconcelos, M.J.P., Mota, B., and Grégoire, J.-M. (2003): The area burned in southern Africa during the 2000 dry season, *J. Geophys. Res.*, 108(D13), 8498,doi:10.1029/2002JD002320.

Silva, J.M.N., Sousa, A.M.O., Pereira, J.M.C., Tansey, K. and Grégoire, J.-M., (2002): A contribution for a global burned area map, in Forest Fire Research and Wildland Fire Safety [CD-ROM], edited by D. X. Viegas, Millpress, Rotterdam.

Simon, M., Plummer, S., Fierens, F., Hoelzemann, J.J. and Arino, O. (2004): Burnt area detection at global scale using ATSR-2: The GLOBSCAR products and their qualification. *Journal of Geophysical Research* 109(D14S02).

Stijn Hantson, Marc Padilla, Dante Corti, & Chuvieco, E. (in review). A Global characterization of MODIS hotspots using high resolution burned area data. *Remote Sensing of Environment*.

Tansey, K., Grégoire, J.M., Defourny, P., Leigh, R., Pekel, J.F., van Bogaert, E. and Bartholomé, E. (2008): A new, global, multi-annual (2000-2007) burned area product at 1 km resolution. *Geophysical Research Letters* 35(L01401): 6.

Tansey, K., Grégoire, J.M., Binaghi, E., Boschetti, L., Brivio, P.A., Ershov, D., Flasse, S., Fraser, R., Graetz, D., Maggi, M., Peduzzi, P., Pereira, J., Silva, J.M.N., Sousa, A.M.O. and Sroppiana, D. (2004): A global inventory of burned areas at 1 Km resolution for the year 2000 derived from SPOT-VEGETATION data. *Climatic Change* **67**(2-3): 345-377.

The ESA Climate Change Initiative – Description issue 1 revision 0 - 30/09/09 EOP-SEP/TN/0030-09/SP (available online at: http://earth.esa.int/workshops/esa_cci/ESA_CCI_Description.pdf

Trigg, S. and Flasse, S. (2001): An evaluation of different bi-spectral spaces for discriminating burned shrub-savannah. International Journal of Remote Sensing, 22, 2641−2647.

Trigg, S. and Flasse, S. (2000): Characterising the spectral-temporal response of burned savannah using in situ spectroradiometry and infrared thermometry. International Journal of Remote Sensing, 21, 3161–3168.

Van der MEER, F.D. (2000): Spectral curve shape matching with a continuum removed CCSM algorithm. International Journal of Remote Sensing 21(16): 3179-3185.